

Extensive Hartree-Fock+BCS calculation with Skyrme SIII force *

Naoki Tajima, Satoshi Takahara, and Naoki Onishi
Institute of Physics, College of Arts and Sciences,
University of Tokyo, Komaba, Meguro, Tokyo, 153, Japan.

Abstract

We have performed deformed Hartree-Fock+BCS calculations with the Skyrme SIII force for the ground states of even-even nuclei with $2 \leq Z \leq 114$ and N ranging from outside the proton drip line to beyond the experimental frontier in the neutron-rich side. We obtained spatially localized solutions for 1029 nuclei, together with the second minima for 758 nuclei. The single-particle wavefunctions are expressed in a three-dimensional Cartesian-mesh representation, which is suitable to describe nucleon skins, halos, and exotic shapes as well as properties of ordinary stable nuclei. After explaining some of the practical procedures of the calculations, we compare the resulting nuclear masses with experimental data and the predictions of other models. We also discuss the quadrupole ($m=0, 2$) and hexadecapole ($m=0, 2, 4$) deformations, the skin thicknesses, the halo radii, and the energy difference between the oblate and the prolate solutions. Our results can be obtained via computer network.

1 Introduction

It is one of the most important goals of the nuclear theory to reproduce and predict the nuclear ground-state energy and other properties globally in the nuclear chart within a single framework. A variety of theoretical models have been introduced for this goal. The most elaborate works have been done in the framework of the finite-range droplet model with a microscopic shell correction (FRDM), whose latest result was given by Möller et al. [1]. Another extensive calculation was carried out by Aboussir et al. [2] in the extended Thomas-Fermi plus Strutinsky integral method (ETFSI). The former as well as the latter methods can be regarded as approximations to the Hartree-Fock (HF) equation. The straight-forward solutions of the equation including deformation require long computation time for global calculations even with present computers. Such global results are not yet available to the public as far as we know. In this paper, we report on the results of our extensive HF+BCS calculation with the Skyrme SIII force for 1029 even-even nuclei having atomic number ranging from 2 to 114 and neutron number from outside the proton drip line to beyond the experimental neutron-rich frontier.

We use a HF+BCS code *EV8* [3], in which the single-particle wavefunctions are expressed in a three-dimensional Cartesian-mesh representation, while most of the other methods for deformed nuclei express the single-particle wavefunctions by the expansion in a harmonic oscillator basis. Let us mention three advantages of the mesh representation. First, it is capable of treating nucleon skins and halos. In contrast, they cannot be described efficiently in the oscillator-basis expansion because the asymptotic form of wavefunctions far from the nuclear surface is determined by the basis. Second, one can treat exotic (e.g., high-multipole) shapes and large

*UT-Komaba 96-9, to be published in Nuclear Physics A

(e.g., super and hyper) deformations without preparing a basis specific to each shape. Third, the saturation property of density makes the atomic nucleus a very suitable object to the mesh representation, as we discuss in section 2.1.

This paper is mainly concerned with the proton-rich nuclei than the neutron-rich ones. We thoroughly explore the proton-rich side, even to beyond the proton drip line by several neutrons, while restricting the investigations in the neutron-rich side within the experimental frontier plus a few neutrons. This is because the HF+BCS method used in this paper cannot correctly include the coupling in the pairing channel with the continuum, which can be influential in nuclei near the neutron drip line[4, 5]. The HF+BCS method including the coupling with the continuum gives rise to unphysical neutron gas surrounding the nucleus. The solution of this problem requires the Hartree-Fock-Bogolyubov method, with which ordinary and pair densities are spatially localized when the Fermi level is at a negative energy[4]. On the other hand, for nuclei near the proton drip line, the HF+BCS method is still applicable in practice to obtain localized solutions because the Coulomb barrier confines the wavefunctions of low-and-positive as well as negative energy levels.

The contents of this paper are as follows. In the next section, we survey the features of the three-dimensional Cartesian-mesh representation, discuss the choice of the interaction, and explain the points newly developed in the present paper for extensive calculations. Among these points are the determination of the pairing force strengths and the acceleration of the convergence to the solution.

In section 3, we compare the atomic masses obtained from our calculations with those in the latest experimental mass table[6]. For this purpose, we consider a correction for the error in the total binding energy due to the finite mesh size: A greatly high precision is necessary in calculating the binding energy compared with other quantities like moments.

Section 4 treats the deformation. We compare the electric axial quadrupole moments with those deduced from the experimental B(E2) \uparrow data[7]. We also discuss the deformation parameters a_{20} , a_{22} , a_{40} , a_{42} , and a_{44} , which we define for the HF+BCS solutions in terms of multipole moments, and compare them with those of the FRDM. The difference of shapes between protons and neutrons as well as the difference of the energies between the prolate and the oblate solutions are also discussed. We choose a shape coexisting nucleus ${}^{80}_{40}\text{Zr}_{40}$ to illustrate the strong dependence on the force parameters of the landscape of the potential energy curve along the axial-quadrupole-deformation path.

The proton and the neutron skins are the subject of section 5. We discuss the thickness, the anisotropy, and the relation with the halo radius.

In the last section, the contents of this paper is summarized and an instruction to obtain our results electronically via computer network is given.

2 The set up of the calculations

2.1 The basis

The main feature of the HF+BCS code *EV8* used in this paper is the three-dimensional Cartesian-mesh representation: Each single-particle wavefunction $\psi(x, y, z)$ is defined in a rectangular box ($-\frac{1}{2}L_x \leq x \leq \frac{1}{2}L_x$, $-\frac{1}{2}L_y \leq y \leq \frac{1}{2}L_y$, $-\frac{1}{2}L_z \leq z \leq \frac{1}{2}L_z$) with its values ψ_{ijk} at cubic mesh points, $(x_i, y_j, z_k) = (i - \frac{1}{2}, j - \frac{1}{2}, k - \frac{1}{2})a$, where i , j , and k take on integers. In this study, the mesh size a is set to 1 fm, while the size of the box is $L_x = L_y = 26$ fm, $L_z = 28$ fm for $Z < 82$ and $L_x = L_y = 28$ fm, $L_z = 30$ fm for $Z \geq 82$. The nucleus is placed at the center of the box.

We impose a symmetry with respect to reflections in x - y , y - z , and z - x planes (the point group D_{2h}). This symmetry allows triaxial solutions, although all of our solutions have eventually turned out axial and stable against γ -deformation. On the other hand, the symmetry prohibits odd-multipole deformations, which may not be negligible in some actinide nuclei. According to

the calculations with the FRDM[1], the nucleus $^{222}_{88}\text{Ra}_{134}$ has the largest octupole deformation ($\beta_3 = 0.15$, the energy gain due to the octupole deformation is -1.4 MeV), while except in the neighborhood of this nucleus the octupole deformation occurs only in odd- A and odd-odd nuclei. Incidentally, both in light[8] and heavy nuclei[9], the octupole deformation is likely to be enhanced by the procedure of the variation after parity projection.

One might wonder that a mesh size of 1 fm were too large to describe the abrupt change of density at nuclear surface. It was demonstrated in Ref. [3], however, that a mesh size $a=1$ fm can produce enough accurate results for several spherical nuclei with mass below ^{208}Pb . We did a similar test of accuracy for a deformed actinide nucleus $^{240}_{94}\text{Pu}_{146}$ and found that the relative errors of the quadrupole moment and the total energy are 0.4% and 0.5%, respectively. (The method of extrapolation to $a \rightarrow 0$ is explained in section 3.1.) This order of accuracy is higher than necessary for the quadrupole moment, while it is not for the energy to make comparison with experiments. Considering that the root-mean-square (r.m.s.) deviation of the atomic masses of recent mass formulae is ~ 0.5 MeV, the desirable precision is of the order of 0.1 MeV, which is only 0.005% of the total binding energy of ^{240}Pu . Therefore, the binding energy, but not the other quantities, has to be corrected for the effect of the finite mesh size, which is done in section 3.1.

The origin of this unexpectedly high accuracy with apparently coarse meshes has been explained by Baye and Heenen[10]. The equation to determine $\{\psi_{ijk}\}$ is usually derived through a discrete approximation to the Schrödinger equation. They presented an alternative point of view, in which they introduced a set of orthogonal basis functions $f_{ijk}(x, y, z)$ such that $\{\psi_{ijk}\}$ are the coefficients to expand $\psi(x, y, z)$ in this basis. (In this point of view, the equation for $\{\psi_{ijk}\}$ is determined uniquely from the variational principle.) This basis can be unitary-transformed to plane-wave basis with $|k_\kappa| < \pi/a$ ($\kappa = x, y, z$), which suggests that the atomic nucleus is a very suitable physical object to apply the mesh representation because the saturation property of nuclear matter guarantees the suppression of large-momentum components in wavefunctions from the view point of the Thomas-Fermi approximation.

To enjoy this high accuracy, the method to determine $\{\psi_{ijk}\}$ must be in accordance with the view point of Baye and Heenen. Exact variational treatment with the plane-wave basis requires, however, long computation time and diminish the simplicity of the Cartesian-mesh representation. The code *EV8* is designed to emulate the plane-wave expansion method, though it is based on the discrete approximations, by choosing the appropriate orders of approximation formulae for derivatives (the 7- and 9-point formulae for the first and second derivatives, respectively) and integrals (the mid-point formula).

It is worth mentioning that a new formulation of the mesh representation in terms of collocation basis splines is being developed recently by Chinn et al.[11].

2.2 The interaction

For the HF (mean-field) part of the interaction, the code uses the Skyrme interaction[12, 13], which is a zero-range force with the lowest order momentum dependences to emulate the finite-range effects, a density dependence to reproduce the saturation of nuclear matter density, and a spin-orbit coupling term.

The relation between the Skyrme-HF model and the relativistic mean-field model[14] has been discussed by many authors (see, e.g., Ref. [15]), which has invoked arguments on the density dependence (the ratio of the isoscalar to the isovector density dependences) of the spin-orbit term[16, 17, 18, 19]. However, as these arguments are not yet conclusive, we rather like to use the old but well-examined standard form of the Skyrme force in this paper.

Among the many parameter sets proposed for the Skyrme force[2, 4, 20, 21, 22, 23, 24, 25, 26], we choose the SIII[20]. Its validity has been examined in many nuclear structure calculations. In particular, it produces single-particle spectra in good agreement with experiment. It also

reproduces fairly well the $N - Z$ dependence of the binding energy[27] compared with other widely-used parameter sets of SGII[23] and SkM*[24]. Although its incompressibility is said to be too large, it is not a serious drawback because elaborate fittings of the parameters of the Skyrme force[19] and the FRDM[1] have shown that different assumptions for the incompressibility lead to practically the same quality of fittings to nuclear masses.

The force SkSC4[2] was determined through the most extensive fitting to nuclear mass data among the Skyrme forces. However, the fitting was done in the ETFSI scheme, which produces unnegligibly different energy from that of the HF method. Because of this disadvantage, we do not choose the force SkSC4 in this paper.

2.3 The pairing

For the interaction in the pairing channel, we employ a seniority force V_{pair}^τ , whose pair-scattering matrix elements are defined as a constant multiplied by cutoff factors depending on the single-particle energy ϵ_i ,

$$\langle i\bar{i}|V_{\text{pair}}^\tau|j\bar{j}\rangle = -G_\tau f_\tau(\epsilon_i)f_\tau(\epsilon_j), \quad (1)$$

where τ signifies proton or neutron. We assume the following form for the cutoff function,

$$f_\tau(\epsilon) = \left\{ 1 + \exp \frac{\epsilon - \epsilon_c^\tau}{0.5 \text{ MeV}} \right\}^{-1/2} \theta(e_c^\tau - \epsilon), \quad (2)$$

which contains two cutoff energies, ϵ_c^τ and e_c^τ : The former is for a smooth cutoff necessary to stabilize the iterative procedures to solve the HF equation, while the latter is for a sharp cutoff preventing occupation of spatially unlocalized single-particle states. The cutoff energies take on the following values,

$$\epsilon_c^\tau = \lambda_{\text{HF}}^\tau + 5 \text{ MeV}, \quad e_c^\tau = \epsilon_c^\tau + 2.3 \text{ MeV}, \quad (3)$$

where λ_{HF}^τ is the Fermi level defined as the average of the highest occupied level and the lowest vacant level in the HF (or normal) state.

In the BCS treatment of nuclei far from the β -stability line, one has to take care so that the continuum states are not occupied, which give rise to unphysical nucleon gas extending over the entire box. In our calculations, for neutrons, if the right-hand side of the second of Eqs. (3) is positive, e_c^τ is replaced by zero (for $Z < 82$) or ϵ_c^τ is replaced by -2.3 MeV (for $Z \geq 82$). For protons, instead of lowering the sharp cutoff energy e_c^τ , we modify the proton potential outside the Coulomb barrier (in the imaginary-time evolution operator, not in the evaluation of the energy) so that the potential is higher than e_c^τ . This prevents the tunneling through the barrier and makes the proton single-particle wavefunctions whose energy is within the pairing active interval ($\epsilon < e_c^\tau$) spatially localized.

In order to treat a wide range of nuclei on a single footing, we need a prescription to determine the strength G_τ for each nucleus. For this purpose, we have developed a method based on the continuous spectrum approximation. We solve the following particle-number and gap equations,

$$N_\tau = \int_{-\infty}^{\infty} \left\{ 1 - \frac{\epsilon - \bar{\lambda}_\tau}{\sqrt{(\epsilon - \bar{\lambda}_\tau)^2 + f_\tau(\epsilon)^2 \bar{\Delta}_\tau^2}} \right\} \bar{D}(\epsilon) d\epsilon, \quad (4)$$

$$\bar{\Delta}_\tau = \frac{G_\tau \bar{\Delta}_\tau}{2} \int_{-\infty}^{\infty} \frac{f_\tau(\epsilon)^2}{\sqrt{(\epsilon - \bar{\lambda}_\tau)^2 + f_\tau(\epsilon)^2 \bar{\Delta}_\tau^2}} \bar{D}(\epsilon) d\epsilon, \quad (5)$$

which use the semiclassical single-particle level density $\bar{D}(\epsilon)$ (obtained in the Thomas-Fermi approximation) instead of the discrete spectrum of the single-particle HF hamiltonian. One notes that $\bar{D}(\epsilon)$ does not have the fluctuation due to the shell effects.

Eq. (4) determines the Fermi level $\bar{\lambda}_\tau$, while Eq. (5) tells the force strength G_τ when it is combined with the empirical formula for the pairing gap $\bar{\Delta}_\tau = 12A^{-1/2}$ MeV. For light nuclei, the resulting G_τ becomes apparently too strong. We replace G_τ with 0.6 MeV when it exceeds 0.6 MeV. The results are discussed in section 3.3.

2.4 The method of solution

Because the single-particle basis of the mesh representation is huge, it takes unmanageably long computation time to solve the HF+BCS equation with the usual method of iterative diagonalization of the single-particle HF hamiltonian h_{HF} . Instead, the code *EV8* employs a much more efficient method of imaginary-time evolution[28], in which the evolution operator for a small time interval Δt is repeatedly operated on each single-particle wavefunction to decrease its expectation value of the energy. After each evolution, the single-particle wavefunctions are orthogonalized in the Gram-Schmidt method from low to high energy states. As the initial wavefunctions, we utilize either the eigenstates of the Nilsson model or the solutions for the neighboring nuclei.

The imaginary-time evolution operator $\exp(-\hbar^{-1}h_{\text{HF}}\Delta t)$ is expanded to the first order in Δt as $1 - \hbar^{-1}h_{\text{HF}}\Delta t$. To this order, the imaginary-time evolution method is equivalent to the gradient iteration method[29]. Consequently, to obtain the minimum energy state rather than the maximum one, it must hold that $1 - \hbar^{-1}\epsilon_{\text{max}}\Delta t > -1$, where ϵ_{max} is the maximum single-particle eigenenergy, which is approximately the free kinetic energy for $k = 3^{1/2}\pi a^{-1}$. With $a=1$ fm, it follows $\Delta t < 2.1 \times 10^{-24}$ sec (The actual upper bound for Δt is larger than this estimation because the discrete approximation underestimates the kinetic energy for very high momentum states). We use $\Delta t = 1.5 \times 10^{-24}$ sec in this paper.

We regard that the wavefunction is converged to a HF+BCS solution when the following four criteria are satisfied.

i) The energy spreading of single-particle states are smaller than 0.1 MeV. Practically, we require that the third largest value of

$$(\Delta\epsilon_i)^2 \equiv \left(\langle i|h_{\text{HF}}^2|i \rangle - \langle i|h_{\text{HF}}|i \rangle^2 \right) \cdot \min \left(2v_i^2, 1 \right) \quad (6)$$

should be less than $(0.1 \text{ MeV})^2$, where $|i \rangle$ represents the i th single-particle state and v_i^2 its BCS occupation probability.

ii) During the last 75 steps of evolution, the variation in the total energy is < 1.5 keV for $Z < 82$ and < 5 keV for $Z \geq 82$.

iii) During the same period, the variation in $\langle x^2 \rangle_\tau$, $\langle y^2 \rangle_\tau$, and $\langle z^2 \rangle_\tau$ are $< 0.5 \text{ fm}^2$ for $Z < 82$ and $< 0.005 \times \frac{1}{5}r_0^2 N_\tau A^{2/3}$ for $Z \geq 82$, where τ stands for all the protons or all the neutrons and $r_0 \equiv 1.2$ fm.

iv) The axial quadrupole deformation parameter δ is close to the convergent value. We adopt a definition $\delta \equiv 3 \langle Q_z \rangle / 4 \langle r^2 \rangle$ [30], where $Q_z \equiv 2z^2 - x^2 - y^2$. The convergent value, δ_{pred} , together with its uncertainty, $\Delta\delta_{\text{pred}}$, are predicted using the values of δ during the last 200 steps¹. The condition is expressed as $|\delta - \delta_{\text{pred}}| + \Delta\delta_{\text{pred}} < 0.004$. For nuclei in the shape-transitional region this criterion is the last one to be satisfied among the four, because the potential energy surface (PES) is very flat versus δ .

In order to accelerate the convergence when the wavefunction looks slowly converging to a state with deformation δ_{pred} , we exert an external mass quadrupole potential during several tens of evolution steps so that the wavefunction quickly acquires the predicted deformation.

¹ In this paper, δ_{pred} is determined by an equation $\dot{\delta}=0$, where $\dot{\delta}$ is the time derivative of δ and expressed as a quadratic function in δ whose coefficients are determined from the least-square fitting to the last n steps. Changing n between 200 and 150 produces a set of values $\{\delta_{\text{pred}}\}$. The average of them is adopted as δ_{pred} , while a half of the difference between the maximum and the minimum of them is used as the size of the error $\Delta\delta_{\text{pred}}$.

Then, we switch off the external potential and continue the free imaginary-time evolution. With this acceleration method, the necessary number of evolution steps to achieve convergence can be decreased by a factor larger than two. The reason why this method works is that the quadrupole deformation is almost always the softest mode in atomic nuclei (under the D_{2h} symmetry). On the other hand, in generic multi-dimensional minimization problems, the principal difficulty is in finding the direction of the softest mode[31].

In the top portion of Fig. 1 we show histories of the imaginary-time evolution of the deformation parameter δ with (solid curve) and without (dot curve) the acceleration method for the prolate solution of $^{156}_{68}\text{Er}_{88}$. The sharp fall of the solid curve is due to the external quadrupole potential exerted between the time steps 213 and 291. One can see that the convergence can be achieved within much shorter time than without the acceleration method.

In the bottom-left and bottom-right portions of the figure, the time evolution of the maximum spreading in the single-particle levels, Eq. (6), and the total energy (measured from the convergent value) are displayed, respectively, for the same process as in the top portion. One can see that the convergence of these quantities are also advanced by using the external potential.

Figure 1

All the solutions of our extensive HF+BCS calculation have been found axially symmetric. The stability of these solutions against triaxial deformation can be known from the time evolution of the (very small) triaxiality parameter when the external potential is not effective, because it should grow exponentially if the axial solution is a saddle point rather than a minimum. It has turned out that none of the axial solutions exhibit clearly such an exponential growth of the triaxiality. It is possible, however, that triaxial minima exist which are separated from the axial path by a potential barrier.

Bonche et al. found triaxial ground-state solutions for ^{84}Zr and ^{94}Zr using the same Skyrme interaction and the same computer code as we used. However, these triaxial minima look so shallow that they can easily be moved to axially symmetric shapes by, e.g., making the pairing correlation slightly stronger.

The treatment of the Coulomb interaction is in line with the appendix C of Ref. [32]: The exchange part of the interaction is approximated by a local potential in terms of the Slater approximation. The direct part is implemented in terms of a Coulomb potential obtained by solving the Poisson equation using a three-point approximation to the second derivative. The boundary conditions are determined by, first, dividing the nucleus into two fragments in one of the x - y , y - z , and z - x planes (we select the plane which gives the largest distance between the centers of mass of the two fragments) and, second, expanding the Coulomb potential originating in each fragment in terms of multipole moments of protons through order three.

Throughout this paper, we treat a nucleon as a point particle, neglecting its extension. The effect of the spurious center of mass motion is corrected for by reducing the bare nucleon mass by a factor $1 - A^{-1}$. The explicit form of the hamiltonian density is found in Ref. [3].

3 The nuclear masses

In the manner described in section 2, we have solved the HF+BCS equation for even-even nuclei with $2 \leq Z \leq 114$. For each isotope chain, the calculation extends from outside the proton drip line by several neutrons to beyond the experimental frontier in the neutron-rich side by a few neutrons. For $Z > 100$, the calculation extends to $N \leq 2Z - 42$. Spatially localized solutions have been obtained for 1029 nuclei. Although some of these solutions have negative two-proton separation energies, their densities are localized owing to the Coulomb barrier. The second local minima have been found for 758 nuclei.

We determine the ground-state solution of each nucleus by, first, searching the spherical, a prolate, and an oblate solutions and, second, comparing the energies of thus obtained solutions. Our strategy to search for these three solutions for each nucleus is as follows. The spherical solution is obtained by constraining the mass quadrupole moments to be zero. The prolate (oblate) solution is searched in two steps. First, we exert an external potential proportional to Q_z on the initial wavefunction until its quadrupole deformation parameter satisfies $\delta > 0.1$ (< -0.1). Second, we switch off the external potential, let the wavefunction evolve by itself (or with the acceleration method described in section 2.4), and see if it converges to a deformed local minimum. If the nuclear shape becomes very close to the sphericity in the course of evolution, i.e. $\delta < 0.02$ (> -0.02), we conclude that the normal-deformation prolate (oblate) solution does not exist in this nucleus.

For some nuclei with $28 < Z, N < 50$, the FRDM[1] predicts very large deformations $\delta \sim 0.4$. In order not to miss such large-deformation solutions, we have done additional searches for all the nuclei in this region, in which we continue to exert the quadrupole potential until δ becomes > 0.4 (< -0.3) before starting the free evolution for the prolate (oblate) solution. These additional searches indeed produced large-deformation solutions. However, none of them are the ground states unlike in the results of the FRDM.

In shape-transitional nuclei, the PES often has more than three normal-deformation minima. However, they are usually very shallow and it is doubtful that each of them corresponds to a distinct eigenstate notwithstanding the quantum fluctuation in shape. Therefore, we do not manage to find out all of these shallow minima.

3.1 Correction for the finite mesh size

As we have discussed in section 2.1, it is necessary to correct the total energy for the inaccuracy due to the finite mesh size because its relative error has to be by far smaller than that of other quantities for the sake of comparison with experimental data.

To evaluate the size of the error, one needs the HF+BCS solution for vanishingly small mesh size. It can be obtained without difficulty concerning spherical solutions, because even personal computers can execute spherical HF+BCS codes with very small radial-grid spacing. Therefore, we have chosen to compare the total energies between the solutions of a spherical HF+BCS code² (the *SKHAFO* taken from Ref. [29]) and the Cartesian-mesh code *EV8* with constraints of vanishing quadrupole moments. In the following, we designate the total energy obtained with the spherical code as E_0 while that from the Cartesian-mesh code simply as E . Our aim is to construct a formula for the energy correction so that the corrected energy $E_c = E + (\text{correction})$ has a much smaller r.m.s. deviation from E_0 than E has.

In the least-square fitting to determine the parameters of the formula, we have used 1005 nuclei (among the 1029 nuclei) whose pairing gaps (both for proton and neutron) coincide within 0.1 MeV between the results of the two codes. With the simplest fitting function of $E_c = E + c_1 A$, the r.m.s. difference between E_c and E_0 can be decreased from 6.7 MeV to 0.35 MeV. By adding terms up to the second order in N and Z ,

$$E_c = E + c_1 A + c_2 (N - Z) + c_3 A^2 + c_4 A (N - Z) + c_5 (N - Z)^2, \quad (7)$$

the r.m.s. value of $E_c - E_0$ is decreased to 114 keV with $c_1 = -40.2$, $c_2 = -20.6$, $c_3 = 0.033$, $c_4 = -0.081$, and $c_5 = -0.080$ (keV). Since this size of error is much smaller than the typical

² The spherical code has been modified such that the following points are the same as in the Cartesian code: the values of physical constants, the treatment of the pairing correlations, and the modification of the proton potential outside the Coulomb barrier. The volume of the spherical cavity was set to the same size as that of the rectangular box used in the Cartesian code. The radial-grid spacing was set at 0.1 fm.

precision of the mass formulae in the market place (~ 0.5 MeV)[1, 2, 33], we have decided to adopt the above formula³.

We have tested the accuracy of the correction formula (7) for deformed solutions by comparing E_c with an energy extrapolated to $a \rightarrow 0$. In the extrapolation, first, we calculate the total energy for seven values of a ranging from 1 fm to 0.56 fm (six values ranging from 1 fm to 0.6 fm for ^{240}Pu), while keeping the box size constant. Second, we fit a polynomial $E(a) = E_{\text{ext}} + b_1 a^2 + b_2 a^6$ to the seven or six sets of values (a, E) using E_{ext} , b_1 , and b_2 as the fitting parameters. This form of the fitting function has been chosen on the following grounds: At $a \sim 1$ fm, the error is dominated by a term of order a^6 , which originates in the seven-point approximation to the first derivatives. At $a \sim 0.5$ fm, the contribution from lower-order terms becomes comparable to that of the a^6 term. These terms seem to arise principally from the error in the Coulomb energy, whose leading order term is a^2 . The ambiguity in the extrapolated energy E_{ext} is roughly estimated to be ~ 0.2 MeV.

In Table 1, the difference between the extrapolated energy to $a \rightarrow 0$ and the energy calculated with $a=1$ fm is shown for oblate, spherical (obtained with constraints of vanishing mass quadrupole moments), and prolate solutions of five nuclei. The fifth column shows the energy correction given by formula (7). For these 15 solutions, the mean and the r.m.s. values of the difference between the correction formula and the extrapolations are 0.0 MeV and 0.21 MeV, respectively, which are smaller than or of the same size as the accuracy of the extrapolation. This agreement shows the applicability of the correction formula (7) to deformed solutions as well as to spherical ones. It also confirms that the spherical code and the Cartesian code with the spherical constraint are indeed equivalent to each other.

Table 1

3.2 Comparison of the masses

Fig. 2 presents the corrected total energies E_c of 1029 even-even nuclei calculated with the HF+BCS method with the Skyrme SIII force⁴. For graphical reason, the smooth (i.e., macroscopic) part E_{macro} has been subtracted, which is defined by fitting functions of the Bethe-Weizsäcker type,

$$E_{\text{macro}} = a_V A + a_S A^{2/3} + a_I (N - Z)^2 A^{-1} + a_C Z^2 A^{-1/3}, \quad (8)$$

to E_c separately for $A < 50$ and $A \geq 50$, varying a_V , a_S , a_I , and a_C as free fitting parameters. The solid (open) circles designate that the nucleus is more (less) bound than the macroscopic trend E_{macro} , while the diameter of each circle is proportional to $|E_c - E_{\text{macro}}|$.

We also show the two-proton (two-neutron) drip lines for the HF+BCS with SIII and for the FRDM[1]. The two-proton (two-neutron) drip line lies between two even-even nuclei whose two-proton (two-neutron) separation energies S_{2p} (S_{2n}) have different signs. As for the two-neutron drip line for the SIII force, we use the macroscopic energy (Eq. (8)) fitted to the SIII results ($a_V = -14.702$ MeV, $a_S = 14.05$ MeV, $a_I = 21.47$ MeV, $a_C = 0.6554$ MeV) because our calculation does not extend to the neutron drip line.

³ Inclusion of higher order terms of N and Z to the correction formula does not substantially decrease the r.m.s. error. With terms of degrees from zero to three (10 terms in total), the r.m.s. error is 107 keV. Addition of up to sixth-order terms (28 terms) leads to an r.m.s. error of 93 keV. On the other hand, addition of only one more term $c_6 E_{\text{TD}} A^{1/3}$ decreases the r.m.s. error to 86 keV, where E_{TD} is the space integral of $B_5 \rho \Delta \rho + B_6 \rho_n \Delta \rho_n + B_6 \rho_p \Delta \rho_p$ (see Ref. [3] for the definitions of B_5 and B_6). Further addition of a term $c_7 (\Delta_n + \Delta_p) A$ reduces the error to 77 keV, where Δ_n and Δ_p are the pairing gaps.

⁴ The nuclear binding energy corresponds to $-E_c$, the nuclear mass to $E_c + Zm_p + Nm_n$, and the atomic mass to $Zm_e - B_e(Z)$ added by the nuclear mass. The values of m_p , m_n , and m_e are taken from Ref. [6]. We use $B_e(Z) = 14.33 Z^{2.39}$ eV. The definitions of energy-related quantities like S_{2p} and S_{2n} are given in Ref. [34].

One can see regions of enhanced stability around double-magic nuclei with $(N, Z) = (50, 50)$, $(82, 50)$, and $(126, 82)$. Another double-magic nucleus $(82, 82)$ is outside the two-proton drip line. The super-heavy double-magic nucleus $(184, 114)$ does not look like a local minimum of nuclear mass in this result.

The two-proton drip lines of the HF+BCS with SIII (solid line) and the FRDM (dash line) are overlapping in most places. The distance between them is $\Delta Z = 4$ for $N = 40$, $\Delta N = 4$ for $Z = 42$ and 78 , and $\Delta Z \leq 2$ and $\Delta N \leq 2$ for the other isotope and isotone chains.

The two-neutron drip lines of the two theoretical approaches are also close to each other. The difference looks of the same size as that between the FRDM and the TUYU mass formula[33], both of which are models whose parameters were determined through extensive fittings to the mass data. This fact indicates the quantitative appropriateness of the macroscopic isospin dependence of the SIII force. Indeed, it is what we expected in choosing the SIII force for our first extensive HF+BCS calculation.

Figure 2

The r.m.s. deviation of the calculated ground-state masses from the experimental ones of 480 even-even nuclei (the best recommended values of Ref. [6] excluding those estimated from systematic trends) is 2.2 MeV. Note that the inaccuracy of calculations due to the finite mesh size remaining after the correction is by far smaller than this deviation.

The difference for each nucleus is shown in Fig. 3. The solid (open) circles are put when the calculated masses are smaller (larger) than the experimental ones, while the diameter of the circles is proportional to the magnitude of the difference. One can see that the calculated masses tend to be overbinding for $Z=8$ and 20 isotopes, and $N=50, 82$, and 126 isotones. Unlike spherical nuclei including these semi-magic isotopes and isotones, deformed nuclei have positive errors, which are ~ 3 MeV rather independently of the size of deformation.

Figure 3

In Table 2, we show the r.m.s. differences of the masses of even-even nuclei between theoretical models as well as between the experiments and the models. In the table, **AW'93** represents the experimental atomic mass table by Audi and Wapstra[6], **TUYU** the mass formula of Tachibana et al. [33], **FRDM** the finite-range droplet model[1], **ETFSI** the extended Thomas-Fermi Strutinsky integral method with the SkSC4 force[2], **EV8C** the HF+BCS results using the Skyrme SIII force with the correction (Eq. (7)), and **macro** the Bethe-Weizsäcker type function fitted to AW'93 ($a_V = -15.280$ MeV, $a_S = 16.01$ MeV, $a_I = 22.33$ MeV, $a_C = 0.6896$ MeV). In parentheses are the number of nuclei to calculate the difference. The r.m.s. deviation from AW'93 is 2.2 MeV for EV8C, which is 3-4 times as large as that of 0.52 MeV for TUYU, 0.68 MeV for FRDM, and 0.74 MeV for ETFSI. It should be noticed, however, that the parameters of FRDM, TUYU, and ETFSI were fitted to all the available recent experimental mass data while the parameters of the SIII force were determined by fitting to the masses and charge radii of only seven spherical nuclei. In addition, the number of the fitting parameters is 275 in TUYU, 19 in FRDM, and 8 in ETFSI, while it is only 6 in the SIII force.

Table 2

As a further investigation of the macroscopic properties of the mass, we examine the possibility to decrease the r.m.s. deviation by improving the macroscopic part of the mass models. Namely, for each combination of the nuclear mass models and the experimental data, we add the Bethe-Weizsäcker type function (Eq. (8)) to one of them and determine the four coefficients to minimize the r.m.s. difference between them. The resulting r.m.s. differences are tabulated

in Table 3. This simple correction method can decrease the r.m.s. error of EV8C from experiments by 27%. As for the other models, however, the improvements are marginal. On the other hand, the differences between the models are greatly decreased because they come predominantly from nuclei near the neutron drip line. This fact suggests that substantial improvements of the macroscopic part of the nuclear mass models are possible only if new experimental mass data of neutron-rich nuclei are provided.

Table 3

3.3 Pairing gaps

Let us compare the experimental and the calculated pairing gaps. The former are calculated by applying the 5-point formula[35] to the experimental masses[6] of nuclei except those at major-shell closures (of protons for the proton gap, of neutrons for the neutron gap), while the latter are obtained directly from the BCS part of the HF+BCS scheme.

When the gaps are plotted versus the mass number A , the experimental ones fall close to the empirical formula $\Delta = 12 A^{-1/2}$ MeV. The calculated gaps also fall near the empirical curve for heavy nuclei but they are raised for $50 < A < 100$. In lighter nuclei ($A < 50$), the calculated gaps are located below the curve, which is due to our setting the maximum pairing force strength to 0.6 MeV. A likely origin of the overestimation for $50 < A < 100$ nuclei is that the pairing active space above the Fermi level (see Eqs. (3)) is smaller than the wavelength of the shell oscillation ($\hbar\omega_{\text{osc}} \sim 41A^{-1/3}$ MeV) for small A ; such a situation does not fit to the continuous spectrum approximation. In future calculations for $A < 100$, it is desirable to improve the method to determine the pairing force strengths.

4 Deformation

Since we impose the reflection symmetries in x - y , y - z , z - x -planes (the D_{2h} symmetry) on our HF+BCS solutions, as explained in section 2.1, our solutions have only multipole moments with even angular momentum l and even magnetic quantum number m .

4.1 quadrupole moments

In Fig. 4, we compare the magnitudes of the intrinsic electric quadrupole moments between our HF+BCS solutions and the experimental values deduced from $B(E2)\uparrow$, i.e., the reduced electric quadrupole transition probability from the ground state to the first excited 2^+ state [7]. This moment is defined for the HF+BCS solutions as

$$Q_0 = \sum_{\text{protons}} \langle 2z^2 - x^2 - y^2 \rangle, \quad (9)$$

where z -axis is the symmetry axis (All of our solutions have practically axial shapes, as described in section 4.2). The deduction of $|Q_0|$ from the $B(E2)\uparrow$ is based on the rigid rotor model [7, 30].

For nuclei with $Q_0 > 3.5$ b, the agreement with experiment is excellent. The even-even nuclei having the largest intrinsic quadrupole moment is ${}^{252}_{98}\text{Cf}_{154}$ (indicated by letter **A** in the figure) in the experimental table[7], while it is ${}^{244}_{106}\text{Rf}_{138}$ among the 1029 HF+BCS solutions ($Q_0=16.6$ b).

The largest discrepancy is found in ${}^{222}_{90}\text{Th}_{132}$ (indicated by **D**), whose experimental Q_0 is 5.5 b while the HF solution is spherical. Two nuclei located at isolated points are ${}^{176}_{78}\text{Pt}_{98}$ (indicated by **B**) and ${}^{222}_{88}\text{Ra}_{134}$ (indicated by **C**).

For nuclei with smaller Q_0 , however, many nuclei falls not in the diagonal line but in a horizontal line, which means that the HF solution has a spherical shape when the experimental

B(E2) \uparrow is not necessarily very small. This may be explained by attributing the enhanced B(E2) \uparrow not only to static deformations but also to the collective shape oscillation around the spherical equilibrium. It may also be related to the complicated landscapes of the potential energy curves of nuclei with $A=50-100$ (see section 4.3).

Figure 4

4.2 Deformation parameters

For certain purposes, the deformation parameters are more useful than the electric multipole moments, although the former are model-dependent while the latter are directly related to the experimental observables. In a widely-used method of the Strutinsky shell correction, the deformation parameters are built in the theory in order to specify the single-particle potential. On the other hand, for mean-field solutions, one has to define the deformation parameters from the density distributions of nucleons.

In this paper, we define the deformation parameters as those of a sharp-surface uniform-density liquid drop which has the same mass moments as the HF+BCS solution has. The mass density of the liquid drop is expressed as

$$\rho(\mathbf{r}) = \rho_0 \theta(R(\hat{\mathbf{r}}) - |\mathbf{r}|), \quad (10)$$

$$R(\hat{\mathbf{r}}) = R_0 \left(1 + \sum_{l,m} a_{lm} Y_{lm}(\hat{\mathbf{r}}) \right). \quad (11)$$

The necessary and sufficient conditions on a_{lm} to fulfill the reality of $R(\hat{\mathbf{r}})$ and the D_{2h} symmetry are that l and m are even numbers and $a_{lm} = a_{lm}^* = a_{l-m}$. We set $a_{lm} = 0$ for $l \geq 6$ and determine the remaining seven parameters ρ_0 , R_0 , a_{20} , a_{22} , a_{40} , a_{42} , and a_{44} such that the liquid drop has the same particle number, mean-square mass radius, and mass quadrupole ($r^2 Y_{2m}$) and hexadecapole ($r^4 Y_{4m}$) moments⁵ as the HF+BCS solution has.

The resulting values of R_0 and a_{20} coincide very well with $(\frac{5}{3})^{1/2} r_{\text{rms}}$ and δ , respectively, where r_{rms} is the r.m.s. radius and δ is the deformation parameter defined in section 2.4. For 5361 samples (mass, proton, and neutron moments of 1029 ground and 758 first-excited solutions), the maximum and the r.m.s. deviations of R_0 from $(\frac{5}{3})^{1/2} r_{\text{rms}}$ are 0.3 fm and 0.06 fm, respectively. Those of a_{20} from a fitted function $(\frac{16}{45}\pi)^{1/2} \delta - 0.47\delta^2 + 0.78\delta^3$ is 0.05 and 0.007, respectively.

The axial quadrupole deformation parameter a_{20} is shown in Fig. 5 for the ground-state solutions of the HF+BCS equation with the SIII force. The open (solid) circles designate prolate (oblate) nuclei, while the diameter of the circles is proportional to the magnitude of the deformation parameter. The two-proton and two-neutron drip lines from our HF+BCS calculations (same as in Fig. 2) are drawn for the sake of convenience.

One can see that nuclei at major-shell closures are spherical except for some $N=28$ isotones, while the deformation develops between the major-shell closures. Such pattern of the development of a_{20} looks regular for $A > 100$, while it is not so regular for $A < 100$, i.e., the change of deformation along isotope or isotone chains is not always smooth. In addition, oblate ground states are embedded here and there in light-mass region while for heavier-mass nuclei they are found only exceptionally in regions near major-shell closures.

The largest deviation from the experimental a_{20} deduced from B(E2) \uparrow occurs in ^{12}C . For this nucleus the experimental B(E2) \uparrow is very large (corresponding to $|a_{20}|=0.59$) and an oblate

⁵ One might wonder that the radial dependence of r^4 so strongly emphasizes the contributions from the peripheral regions that the deformation is sensibly affected by the shape of the box. To see the size of such erroneous effects we have done calculations by changing the radial dependence of the hexadecapole moment from r^4 to r^2 in the determination of the deformation parameters. The resulting values of a_{lm} are only marginally changed except in a few nuclei outside the proton drip line. Incidentally, the FORTRAN source code to determine the seven liquid-drop parameters is obtainable via computer network. See an explanation at the end of this paper.

intrinsic deformation with a triangular three-alpha-cluster configuration has been suggested. Indeed, calculations using the Nilsson model[36] and the Strutinsky method[37] give oblate ground states. On the other hand, the HF+BCS calculation with the SIII force gives a potential energy curve which has only one minimum at the spherical shape. Other widely-used Skyrme forces of the SkM* and the SGII also give the only minimum at sphericity, while an old Skyrme force SII gives an oblate minimum with $\delta = -0.27$ [38]. However, one cannot deduce the superiority of the SII force since the optimal shapes of light nuclei are apt to be changed when effects beyond mean-field approximations are taken into account. For example, the parity projection may be important[8] because the triangular three-alpha-cluster configuration violates the symmetry.

A comparison with the results of the FRDM[1] indicates a systematic differences in $Z \sim N \sim 40$ region, where our solutions tend to predict smaller deformations than those of the FRDM. We discuss on this difference in section 4.3. Another systematic difference occurs in a long and narrow region close to the proton drip line with $94 \leq Z \leq 102$, where the FRDM predicts oblate shapes while our calculations give small prolate shapes, on which we do not discuss in this paper.

Figure 5

Deformations with the magnetic quantum number $m=2$ (triaxial deformations) are almost vanishing for all the nuclei we calculated: The magnitudes of a_{22} and a_{42} are smaller than 10^{-4} . The deformation with $m=4$ (a_{44}) is larger than those with $m=2$. Its typical size is of the order of 10^{-3} and the sign is mostly negative. However, these small non-axial deformations cannot affect any observables in experimentally detectable ways. Incidentally, it is an interesting problem how a_{44} develops as the angular momentum increases[39].

The axial hexadecapole deformation parameter a_{40} is shown in Fig. 6 in the similar manner as in Fig. 5. This parameter becomes sizable for $Z > 50$. The sign of a_{40} is positive in the first half of the major shells and negative in the second half. This behavior is in agreement with the results of the FRDM[1] as well as with a naive expectation from the density profile of pure- j single-particle wavefunctions. The largest value of $|a_{40}|$ is about 0.1 both for positive and negative signs.

Figure 6

One of the advantages of mean-field methods over shell-correction schemes is that the protons and the neutrons do not have to possess the same radius and deformation. Making use of this advantage, we have calculated the liquid-drop shape parameters separately for protons and neutrons for 1029 ground and 758 first-excited solutions. As for a_{20} , the r.m.s. difference between protons and neutrons is 0.012, while the maximum difference occurs in the ground state of ${}^{14}_4\text{Be}_{10}$ ($a_{20}^{\text{pro}} = 0.52$, $a_{20}^{\text{neu}} = 0.36$). The absolute value of the difference is smaller than 0.05 for 98.9 % of the solutions. For a_{40} , the r.m.s. difference is 0.0063, while the maximum difference is found in ${}^{16}_4\text{Be}_{12}$ ($a_{40}^{\text{pro}} = -0.03$, $a_{40}^{\text{neu}} = -0.13$). Concerning R_0 , the r.m.s. difference is 0.18 fm. The maximum difference excluding nuclei outside the drip lines occurs again in ${}^{16}\text{Be}$ ($R_0^{\text{pro}} = 3.0$ fm, $R_0^{\text{neu}} = 3.9$ fm). To summarize, the shapes of proton and neutron density distributions are not remarkably different from each other in any of our solutions. As for the radius, we also study the difference at much lower densities, i.e., skins and halos, in section 5.

4.3 $28 < Z, N < 50$ nuclei

Our calculations tend to predict smaller deformations than the FRDM[1] for nuclei in $28 < Z, N < 50$. These discrepancies in deformation often occur in a manner that our model gives a spherical shape while the FRDM predicts $\delta \sim 0.4$. These are originated in shape coexistence, i.e., the potential energy curve has more than one minimum which are energetically competing within ~ 1 MeV.

As an example to illustrate such a subtle situation, we take up ${}^{80}_{40}\text{Zr}_{40}$, for which the FRDM predicts a large prolate deformation $a_{20}=0.43$ while our calculation gives a moderate oblate deformation. In Fig. 7 the solid curve represents the potential energy curve calculated with the SIII force. It has as many as three minima, i.e., an oblate one at $\delta = -0.18$, almost spherical one, and a prolate one at $\delta = 0.41$. Because the energies of these three minima are so close to each other (they are within 0.6 MeV), the order of the energies can be altered easily by changing the parameters of the interaction. With our chosen parameters, the oblate minimum has the lowest energy (solid curve). If one decreases the pairing gap by 25% (i.e., the average pairing gap $\bar{\Delta}_\tau$ with which to determine the pairing force strength is changed from $12 A^{-1/2}$ MeV to $9 A^{-1/2}$ MeV) the prolate minimum becomes the ground state (dot curve). Instead, by changing the Skyrme force parameter set to the SkM*, while using the standard pairing force strength, one can make the prolate minimum the ground state (dash curve). On the contrary, the SGII force deepens the spherical minimum (dot-dash curve). The shapes of nuclei in this mass region have been studied in many papers[40, 41, 42, 43].

Figure 7

4.4 Oblate solutions

In Fig. 8, the energy differences between the oblate and the prolate solutions are plotted versus the neutron number. We put circles for those nuclei which have both the prolate and the oblate local minima. The circles belonging to the same isotope chain are connected by a line to guide the eyes.

The energy difference is small near major-shell closures but large in the middle of the major shells. Apart from this shell fluctuation, one can see some overall trends. For each of the three major shells of neutrons divided by $N=50, 82, 126$, and 184 , the largest energy difference is 4.70 MeV (${}^{124}_{62}\text{Sm}_{62}$, $\delta=-0.25, 0.37$), 6.58 MeV (${}^{164}_{64}\text{Gd}_{100}$, $\delta=-0.22, 0.31$), and 11.05 MeV (${}^{254}_{102}\text{No}_{152}$, $\delta=-0.17, 0.26$), respectively; as the nucleus becomes heavier, the energy difference increases while the size of deformation decreases.

For nuclei with $N < 50$, the changes along isotope chains are not so regular as in heavier nuclei and the oblate solutions often have lower energies than prolate ones. For nuclei with $N > 50$, oblate ground states are very rare and found only in nuclei very close to shell magics. The dominance of prolate deformations for $N > 50$ may be attributed to the change of the nature of the major shells from the harmonic-oscillator shell to the Mayer-Jensen shell.

Figure 8

5 nucleon skins

As discussed in section 1, the greatest advantage of the mesh representation for this paper is that it is fit to describe skins and halos.

We choose to define the skin by two conditions: A point \mathbf{r} is in the proton or neutron skin when

$$\rho_\tau(\mathbf{r}) > \frac{3}{4}\rho_{\text{tot}}(\mathbf{r}) \quad \text{and} \quad \rho_{\text{tot}}(\mathbf{r}) > \frac{0.16 \text{ fm}^{-3}}{100}, \quad (12)$$

where τ specifies proton or neutron and “tot” stands for proton+neutron. A similar definition was given in Ref. [44]. The value of 0.16 fm^{-3} is chosen as a standard density of the nuclear matter. Since the factors $\frac{3}{4}$ and $\frac{1}{100}$ in the above definitions could have been differently chosen in rather arbitrary fashions, the absolute sizes of the skin thickness do not have a very precise meaning. Nevertheless, these values are useful to judge how the nucleon skins develop as the nucleus approaches to the drip line in the nuclear chart.

Fig. 9 presents the nucleon skin thicknesses calculated according to the above definition⁶. We put an open (solid) circle if the proton (neutron) skin exists for each nucleus. The diameter of the circle is proportional to the skin thickness. Among even-even nuclei inside the proton drip line, only nine have the proton skin (the heaviest one is ${}^{46}_{26}\text{Fe}_{20}$). Proton skins thicker than 1 fm are found in ${}^{12}_8\text{O}_4$ (1.3 fm), ${}^6_4\text{Be}_2$ (1.2 fm), and ${}^{22}_{14}\text{Si}_8$ (1.1 fm), all of which are single-magic spherical nuclei. On the other hand, the neutron skin has non-zero thickness in 39% of the 1029 nuclei which we have calculated. In middle-weight nuclei ${}^{134}_{50}\text{Sn}_{84}$ and ${}^{136}_{50}\text{Sn}_{86}$, between which the present experimental neutron-rich frontier passes[45], the neutron skin is as thick as 1.02 fm and 1.19 fm, respectively. The growth of the skin along isotope and isotone chains is monotonous and have no irregularity irrespective of proton or neutron and both inside and outside the proton drip line.

Figure 9

When the nucleus is deformed, the thickness of the skin depends on the direction. (In Fig. 9, we take the arithmetic average of the thicknesses in the x -, y - and z -axes.) The ratio of the difference between the maximum and the minimum among the three axes to the average over the three axes is 8% for the proton skins and 20% for the neutron skins on the average. The relation between the anisotropy of the skin thickness and the quadrupole deformation parameter δ is shown in Fig. 10. For each ground or first-excited solution having nucleon skins, a symbol is put at a point whose abscissa is δ and its ordinate the skin thickness in the symmetry axis subtracted by that in the equatorial plane. The solid line is the result of a least-square fitting, while two dash lines correspond to twice as large mean-square deviation as the minimum value and can be used to judge the quality of the fitting. For neutron skins, there is a tendency that the skin is thicker in the symmetry axis than in the equatorial plane for oblate deformations and vice versa for prolate deformations: The neutron skin tends to make density more spherical. For protons, it is an interesting question whether the Coulomb repulsion between protons can reverse the trend in such a way that the proton skin promotes deformation. However, one cannot see any clear tendency in the right-hand side of Fig. 10, mainly because the number of points are fewer (heavy nuclei do not have proton skins).

Figure 10

The nucleon halo, being composed of only two nucleons, has much lower density than the nucleon skin. We define the halo radius as the largest r satisfying the following condition,

$$\rho_{\text{tot}}(r) \geq \frac{0.16 \text{ fm}^{-3}}{10000}, \quad (13)$$

where $\rho_{\text{tot}}(r)$ is the angle-averaged mass density. Let us also define the halo thickness as the halo radius subtracted by 1.2 $A^{1/3}$ fm. According to these definitions, the halo radius (thickness) in the salient case of ${}^{11}_3\text{Li}_8$ is 11.2 fm (8.5 fm) while the neutron skin thickness defined by Eqs. (12) is only 1.9 fm (from Fig. 4 of Ref. [46] and Fig. 4 of Ref. [47]). In Fig. 11, we show the relation between the skin and the halo thicknesses. One can see that the halo grows much slower than the skin for thin-skin nuclei (i.e. near the β -stability line) but by far faster for thick-skin nuclei (i.e. near the drip lines). The maximum value of the halo thickness is 6.9 fm of ${}^{50}_{16}\text{S}_{34}$ (indicated

⁶ In the mesh representation, the density is given only at the mesh points. In order to calculate the skin thickness in the x -axis more accurately than the mesh spacing, first, we interpolate the density at the points of intersections between the x -axis and the mesh planes $x = (i + \frac{1}{2})a$ using polynomials of order two in y^2 and z^2 . Second, interpolations to arbitrary points in the x -axis are done for the logarithm of the density using polynomials of order three in x . The resulting density in logarithmic plots versus x shows no artificial ripples due to the interpolations.

by letter **C** in the figure) among the nuclei inside the drip lines. This value is somewhat smaller than 8.5 fm of ^{11}Li . One should note, however, that such a large halo as in ^{11}Li can be formed only in a very restricted interval of the last-occupied nucleon level[47]. It is possible that more gigantic halos are produced for different force parameters.

Figure 11

6 Summary

In this paper we have presented the results of our extensive Hartree-Fock+BCS calculations with the Skyrme SIII force for 1029 even-even nuclei with $2 \leq Z \leq 114$ from outside the proton drip line by several neutrons to beyond the experimental neutron-rich frontier by a few neutrons.

The single-particle wavefunctions are expressed in a three-dimensional Cartesian-mesh representation, whose advantages for atomic nuclei have been discussed. We have explained the newly developed points of the method of calculation, including the determination of the pairing force strengths, the acceleration of the convergence to the HF+BCS solution using an external quadrupole potential, and the correction of the total energy for the finite mesh size.

We have compared the calculated ground-state masses with experimental data and with predictions by other mass models in section 3. The error from experiment is negative for most of spherical nuclei, while for deformed nuclei it is ~ 3 MeV rather independently of the size of deformation. The r.m.s. value of the error for 480 even-even nuclei is 2.2 MeV, which is much larger than the precision (~ 0.5 MeV) of recent extensively-parameter-fitted mass models like the TUIY and the FRDM. However, the proton drip line in the nuclear chart is almost identical to that of the FRDM. Even the location of the neutron drip line is not very distant from that of the FRDM and the TUIY.

Deformations are discussed in section 4. Because of the D_{2h} symmetry imposed on the solutions, only even electric multipole moments do not vanish. We have compared the electric intrinsic axial quadrupole moments of our solutions with those deduced from experimental $B(E2)\uparrow$. The agreements between them are good except those nuclei with small quadrupole moments. After defining the deformation parameters a_{lm} for the HF+BCS solutions in terms of multipole moments, we have plotted the resulting a_{20} and a_{40} in the (N, Z) plane. The magnitudes of non-axial deformation parameters a_{22} , a_{42} , and a_{44} have turned out very small ($|a_{22}|$, $|a_{42}| < 10^{-4}$, $|a_{44}| \sim 10^{-3}$). The difference of shapes between protons and neutrons have been found small, too. Detailed discussions have been presented for ^{12}C and ^{80}Zr . We have also shown the excitation energy between the oblate and the prolate solutions and pointed out a clear difference between below and above the $N = 50$ shell magic.

Nucleon skins are discussed in section 5. We have shown that the skin grows monotonously and regularly as nucleons are added to the nucleus. On the other hand, the halo grows very slowly except near the drip lines, where it changes the behavior completely and expands very rapidly. It has also been found that the neutron skin tends to make the density distribution more spherical.

Among the future problems for the extensive mean-field calculations of the nuclear ground-states properties are the improvements of the method to determine the pairing force strengths and the extension of the calculation to the neutron drip line by incorporating the coupling to the continuum in the pairing channel. Our final goal is the comparison of various Skyrme forces in their ability to reproduce the nuclear ground-state properties globally in the nuclear chart, and possibly the improvements of the force parameters.

All the results of the extensive HF+BCS calculations reported in this paper are available electronically as an anonymous ftp service on the internet: **nt1.c.u-tokyo.ac.jp**. See a file

read.me in the home directory for instructions. The available quantities are the binding energies, the Fermi levels, the pairing gaps, proton and neutron moments (r^2 , $r^2Y_{2,0}$, $r^2Y_{2,2}$, $r^4Y_{4,0}$, $r^4Y_{4,2}$, $r^4Y_{4,4}$), the skin thicknesses, the halo radii, and the proton/neutron/mass deformation parameters (a_{20} , a_{22} , a_{40} , a_{42} , a_{44} , R_0 , ρ_0) of 1029 ground states and 758 first-excited local minima. Single-particle spectra and density distributions of protons and neutrons are also obtainable for each solution. Additional postscript figures and some FORTRAN source codes to analyze the results are also provided.

Acknowledgements

The authors thank Dr. P. Bonche, Dr. H. Flocard, and Dr. P.-H. Heenen for providing the HF+BCS code *EV8*. They are also grateful to Dr. T. Tachibana and Dr. K. Oyamatsu for the TUYU mass formula code, to Dr. S. Raman for supplying the computer file of the B(E2) \uparrow table, and to Dr. P. Möller, Dr. Dobaczewski, and Dr. Nazarewicz for discussions. This work was financially supported by RCNP, Osaka University, as RCNP Computational Nuclear Physics Project (Nos. 94-B-01 and 95-B-01). Part of the calculations were performed with a computer VPP500 at RIKEN (Research Institute for Physical and Chemical Research, Japan).

References

- [1] P. Möller, J.R. Nix, W.D. Myers, and W.J. Swiatecki, Atomic Data Nucl. Data Tables **59** (1995) 185.
- [2] Y. Aboussir, J.M. Pearson, A.K. Dutta, and F. Tondeur, Nucl. Phys. **A549** (1992) 155; Atomic Data Nucl. Data Tables **61** (1995) 127.
- [3] P. Bonche, H. Flocard, P.-H. Heenen, S.J. Krieger, and M.S. Weiss, Nucl. Phys. **A443** (1985) 39.
- [4] J. Dobaczewski, H. Flocard, and J. Treiner, Nucl.Phys. **A422** (1984) 103.
- [5] J. Dobaczewski, I. Hamamoto, W. Nazarewicz, and J.A. Sheikh, Phys. Rev. Lett. **72** (1994) 981.
- [6] G. Audi and A.H. Wapstra, Nucl.Phys. **A565** (1993) 1.
- [7] S. Raman, C.H. Malarkey, W.T. Milner, C.W. Nestor, JR., and P.H. Stelson, Atomic Data Nucl. Data Tables **36** (1987) 1.
- [8] Y. Kanada-En'yo and H. Horiuchi, Prog. Theor. Phys. **93** (1995) 115.
- [9] P. Bonche, S.J. Krieger, M.S. Weiss, J. Dobaczewski, H. Flocard, P.-H. Heenen, Phys. Rev. Lett. **66** (1991) 876.
- [10] D. Baye and P.-H. Heenen, J. Phys. **A19** (1986) 2041.
- [11] C.R. Chinn, A.S. Umar, M. Vallières, and M.R. Strayer, preprint nucl-th.9410034, to be published in Phys. Rep.
- [12] T.H.R. Skyrme, Phil. Mag. **1** (1956) 1043.
- [13] D. Vautherin and D.M. Brink, Phys. Rev. **C5** (1972) 626.
- [14] P.-G. Reinhard, Rep. Prog. Phys. **52** (1989) 439.
- [15] K. Sumiyoshi, D. Hirata, H. Toki, and H. Sagawa, Nucl. Phys. **A552** (1993) 437.
- [16] M.M. Sharma, G.A. Lalazissis, W. Hillebrandt, and P. Ring, Phys. Rev. Lett. **72** (1994) 1431.
- [17] J. Dobaczewski and W. Nazarewicz, Phys. Rev. Lett. **73** (1994) 1869.

- [18] J.M. Pearson and M. Farine, Phys. Rev. **C50** (1994) 185.
- [19] P.-G. Reinhard and H. Flocard, Nucl. Phys. **A584** (1995) 467.
- [20] M. Beiner, H. Flocard, Nguyen van Giai, and P. Quentin, Nucl.Phys. **A238** (1975) 29.
- [21] H.S. Köhler, Nucl. Phys. **A258** (1976) 301.
- [22] H. Krivine, J. Treiner, and O. Bohigas, Nucl.Phys. **A336** (1980) 155.
- [23] Nguyen van Giai and H. Sagawa, Phys.Lett **B106** (1981) 379.
- [24] J. Bartel, P. Quentin, M. Brack, C. Guet, and H.-B. Hakansson, Nucl.Phys. **A386** (1982) 79.
- [25] M. Waroquier, K. Heyde, and G. Wenes, Nucl. Phys. **A404** (1983) 269, 298.
- [26] J.M.G. Gómez, C. Prieto, and J. Navarro, Nucl. Phys. **A549** (1992) 125.
- [27] N. Tajima, P. Bonche, H. Flocard, P.-H. Heenen, and M.S. Weiss, Nucl. Phys. **A551** (1993) 434.
- [28] K.T.R. Davies, H. Flocard, S. Krieger, and M.S. Weiss, Nucl. Phys. **A342** (1980) 111.
- [29] P.-G. Reinhard, in “Computational Nuclear Physics 1”, ed. K. Langanke, J.A. Maruhn, and S.E. Koonin, (Springer-Verlag, Berlin, 1991) 28.
- [30] A. Bohr and B.R. Mottelson, *Nuclear Structure*, vol. 2, (Benjamin, New York, 1975).
- [31] W.H. Press, B.P. Flannery, S.A. Teukolsky, and W.T. Vetterling, *Numerical Recipes* (Cambridge Univ. Press, 1989).
- [32] H. Flocard, S.E. Koonin, and M.S. Weiss, Phys. Rev. **C17** (1978) 1682.
- [33] T. Tachibana, M. Uno, M. Yamada, and S. Yamada, Atomic Data Nucl. Data Tables **39** (1988) 251.
- [34] G. Audi and A.H. Wapstra, Nucl.Phys. **A565** (1993) 66.
- [35] D.G. Madland and J.R. Nix, Nucl.Phys. **A476** (1988) 1.
- [36] A.B. Volkov, Nucl. Phys. **74** (1965) 33.
- [37] G. Leander, S.E. Larsson, Nucl. Phys. **A239** (1975) 93.
- [38] D. Vautherin, Phys.Rev.**C7** (1973) 296.
- [39] I. Hamamoto and B. Mottelson, Phys. Lett. **B333** (1994) 294.
- [40] M. Girod, J.P. Delaroche, D. Gogny, and J.F. Berger, Phys. Rev. Lett. **62** (1989) 2452.
- [41] D.C. Zheng, L. Zamick, Phys. Lett. **B266** (1991) 5.
- [42] J.P. Maharana, Y.K. Gambhir, J.A. Sheikh, P. Ring, Phys. Rev. **C46** (1992) R1163.
- [43] E. Kirchuk, P. Federman, S. Pittel, Phys. Rev. **C47** (1993) 567.
- [44] N. Fukunishi, T. Otsuka, and I. Tanihata, Phys. Rev. **C48** (1993) 1648.
- [45] Yu.V. Sergeenkov, Nucl. Data Sheets **71** (1994) 557.
- [46] Y. Tosaka and Y. Suzuki, Nucl. Phys. **A512** (1990) 46.
- [47] H. Sagawa, Phys. Lett. **B286** (1992) 7.

TABLES

Table 1. Estimated errors of the total energy due to the finite mesh size of $a=1$ fm for oblate, spherical, and prolate solutions of five nuclei in MeV. The sign of the errors are inverted. The last column shows the values given by the correction formula (7). See text for explanations.

	oblate	spherical	prolate	correction
$^{72}_{34}\text{Se}_{38}$	2.9	3.1	2.8	2.83
$^{100}_{40}\text{Zr}_{60}$	4.4	4.7	4.2	4.30
$^{130}_{60}\text{Nd}_{70}$	4.9	5.1	4.7	4.99
$^{170}_{68}\text{Er}_{102}$	7.1	7.3	6.7	7.14
$^{240}_{94}\text{Pu}_{146}$	10.1	10.0	9.9	10.05

Table 2. The r.m.s. differences of nuclear masses between experiment and theoretical models and between theoretical models in MeV. In parentheses are the number of even-even nuclei to take the mean value. The FRDM (the ETFSI) does not give masses for $N < 8$ or $Z < 8$ (for $A < 36$), while AW'93 and EV8C do not extend to the neutron drip line. See text for explanations.

	AW'93	TUYY	FRDM	ETFSI	EV8C
TUYY	0.52 (480)				
FRDM	0.68 (462)	4.31 (1521)			
ETFSI	0.74 (430)	4.27 (1472)	2.74 (1742)		
EV8C	2.22 (480)	2.59 (977)	2.50 (958)	2.26 (940)	
macro	3.55 (480)	17.25 (2228)	16.07 (2246)	8.29 (1895)	5.71 (1029)

Table 3. Same as in Table 2, but the r.m.s. errors have been decreased by adding Bethe-Weizsäcker type functions to the models. See text for explanations.

	AW'93	TUYY	FRDM	ETFSI
TUYY	0.50			
FRDM	0.68	1.73		
ETFSI	0.68	1.53	2.10	
EV8C	1.62	1.80	1.57	1.54

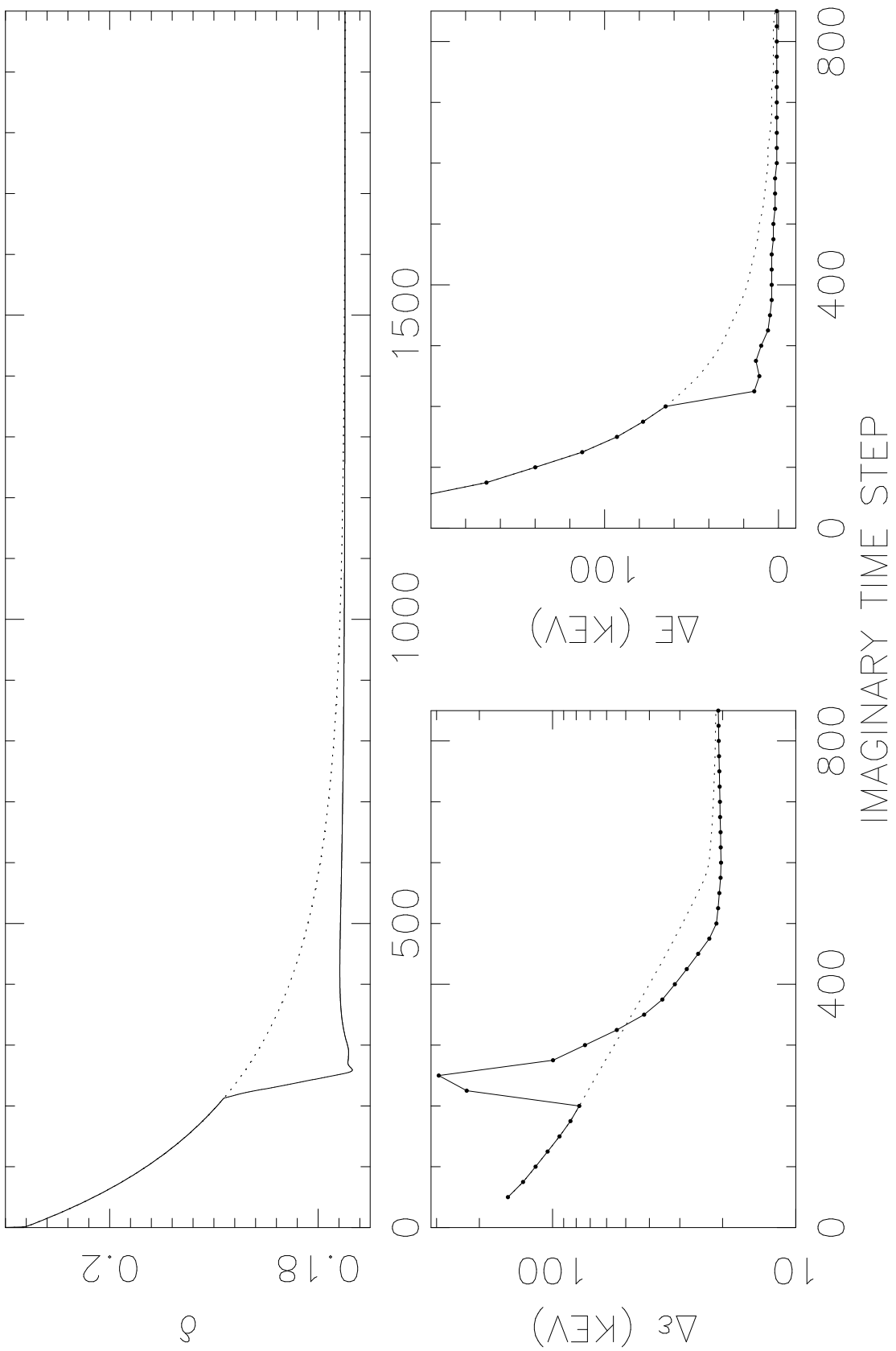
FIGURE CAPTIONS

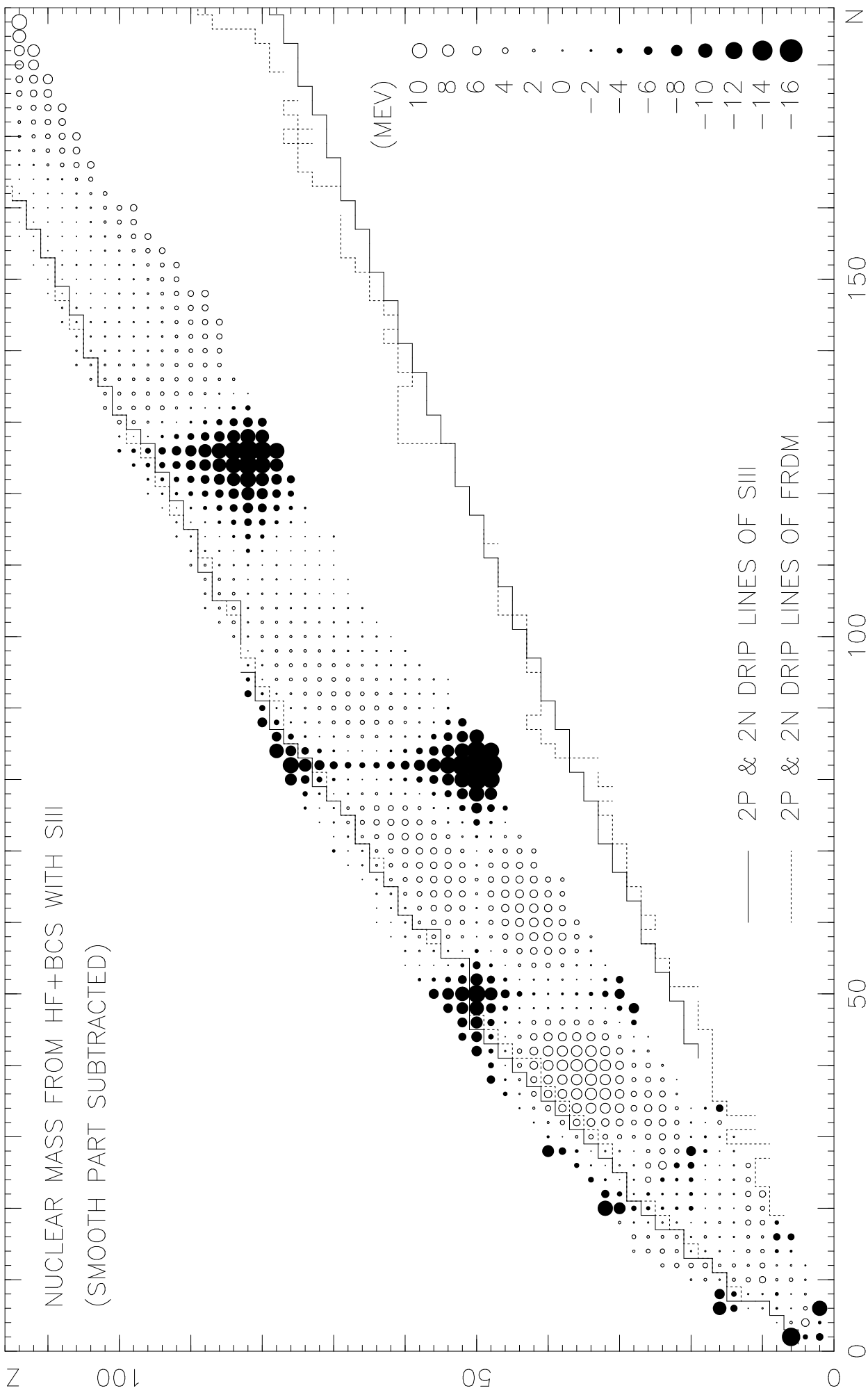
- Fig. 1. Imaginary-time evolution of the deformation parameter δ (top portion), the maximum energy spreading of the single-particle states $\Delta\epsilon$ (bottom-left portion), and the total energy relative to the convergent value ΔE (bottom-right portion) for ^{156}Er . The initial single-particle wavefunctions are taken from those of the HF+BCS solution for ^{158}Er . The abscissae of the three graphs represent the number of steps of the imaginary-time evolution. The dot curves represent the history of a free evolution while the solid curves are obtained by switching on an external quadrupole potential between time steps 213 and 291 to accelerate the convergence. The quantity δ is calculated in every step, while $\Delta\epsilon$ and ΔE are in every 25 steps.
- Fig. 2. Nuclear masses calculated with the HF+BCS with SIII corrected according to Eq. (7). The smooth part of Bethe-Weizsäcker form has been subtracted. The solid staircase-like lines designate two-nucleon drip lines from our calculations. The dash lines are those from the FRDM[1].
- Fig. 3. Error of the nuclear masses calculated with the HF+BCS with SIII corrected according to Eq. (7). The grid indicates the locations of the magic numbers.
- Fig. 4. Comparison between the experimental and the calculated intrinsic quadrupole moments in unit of barn. For each nucleus whose $B(E2)\uparrow$ is given in Ref. [7] (289 even-even nuclei ranging over $4 \leq Z \leq 98$), a dot is put at a point whose abscissa is equal to the experimental value and its ordinate to the value calculated with the HF+BCS with SIII. The diagonal line is drawn so that one can see easily the quality of the agreement. See text for explanations.
- Fig. 5. The quadrupole deformation parameter a_{20} of the ground state solutions of the HF+BCS with SIII for even-even nuclei. Prolate (oblate) nuclei are designated with open (solid) circles whose diameter is proportional to $|a_{20}|$. The staircase-like lines represent two-nucleon drip lines from our calculations.
- Fig. 6. Same as in Fig. 5, but for the hexadecapole deformation parameter a_{40} . The grid indicates the locations of the magic numbers.
- Fig. 7. The potential energy curves for ^{80}Zr obtained by solving the HF+BCS equation with constraint on the mass quadrupole moment Q_z . The abscissa is the deformation parameter δ , while the ordinate is the energy without correction for the finite-mesh-size effect. The solid and the dot curves are calculated with the SIII force, the former with the standard-strength and the latter with a weaker pairing correlation. The dash curve is calculated with the SkM* force, while the dot-dash curve with the SGII force (vertically shifted by 15 MeV).
- Fig. 8. The energy difference between the oblate and the prolate solutions of the HF+BCS with SIII. The abscissa is the neutron number N , while the ordinate is the energy of the oblate solution subtracted by that of the prolate solution. A circle is put only when both solutions exist for each nucleus. The circles belonging to the same isotope chain are connected by a line to guide the eyes. The atomic number Z can be known from the direction of the hand in each circle.
- Fig. 9. The thickness of the proton and the neutron skins of the ground states of the HF+BCS with SIII. The proton (neutron) skin thickness is proportional to the diameter of open (solid)

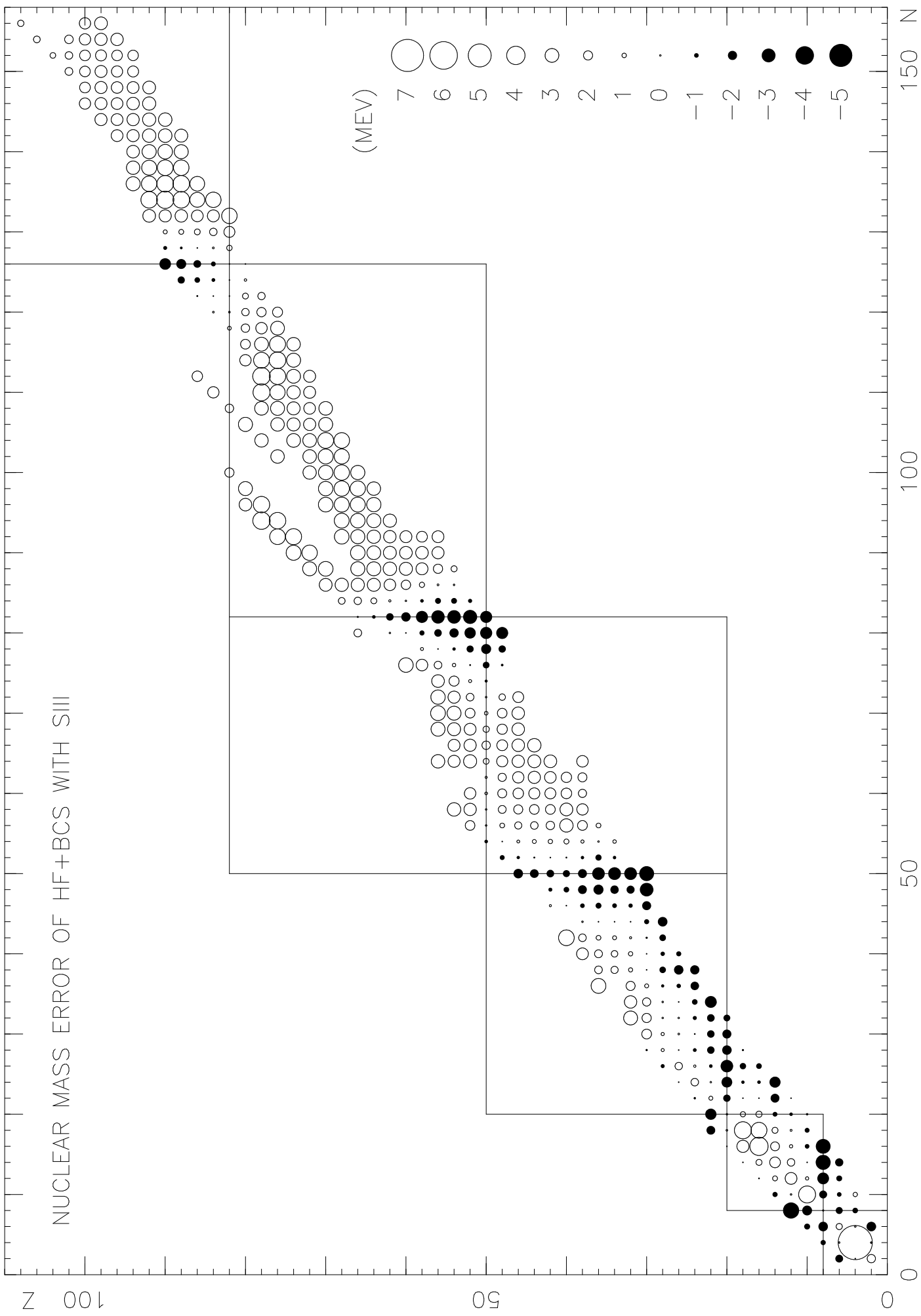
circles. The staircase-like lines represent two-nucleon drip lines from our calculations.

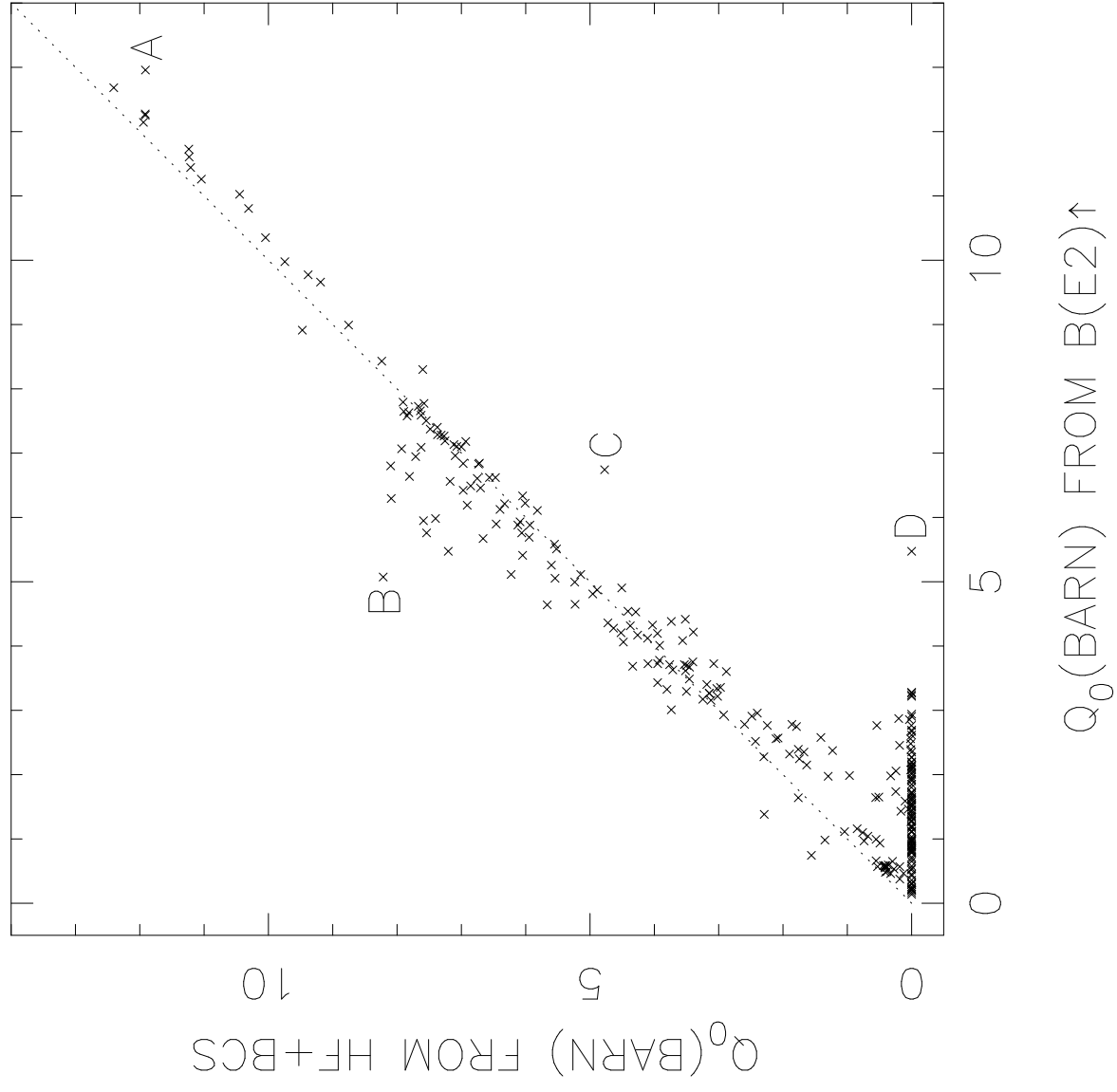
Fig. 10. The dependence of the anisotropy of the proton and the neutron skins on the quadrupole deformation parameter δ . The circle (plus) symbol is used for nuclei with $A \leq 100$ (> 100). See text for explanations.

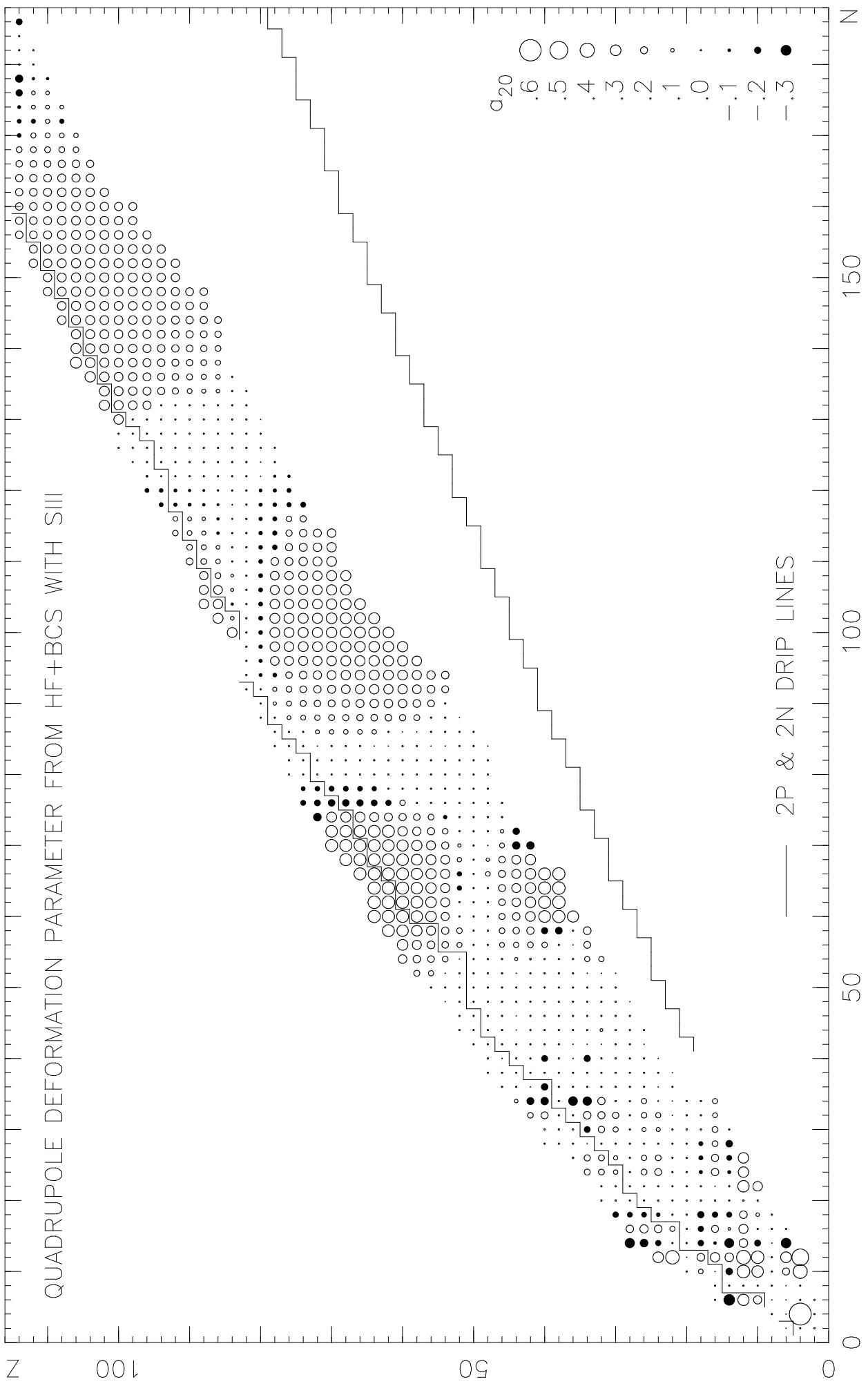
Fig. 11. The relation between the thicknesses of halos and skins. For each of the ground and first-excited solutions of even-even nuclei, a plus symbol is plotted when the skin is of protons or there is no skins, while an x symbol is put when the skin is of neutrons. The plus symbols indicated by letters **A** and **B** correspond to ${}^{22}_{16}\text{S}_6$ and ${}^{20}_{14}\text{Si}_6$, respectively, which are outside the proton drip line. The x symbol indicated by letter **C** corresponds to ${}^{50}_{16}\text{S}_{34}$.

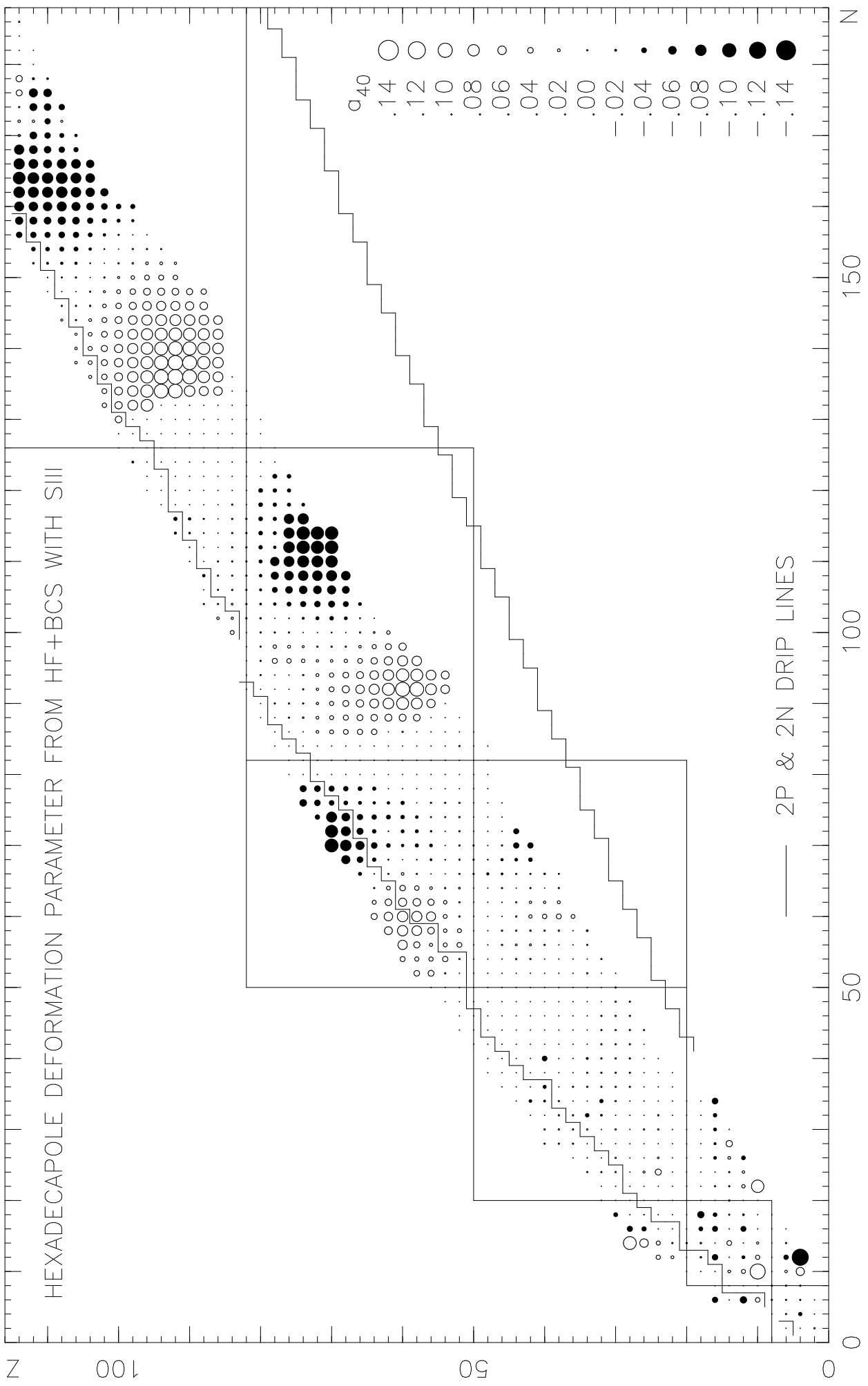


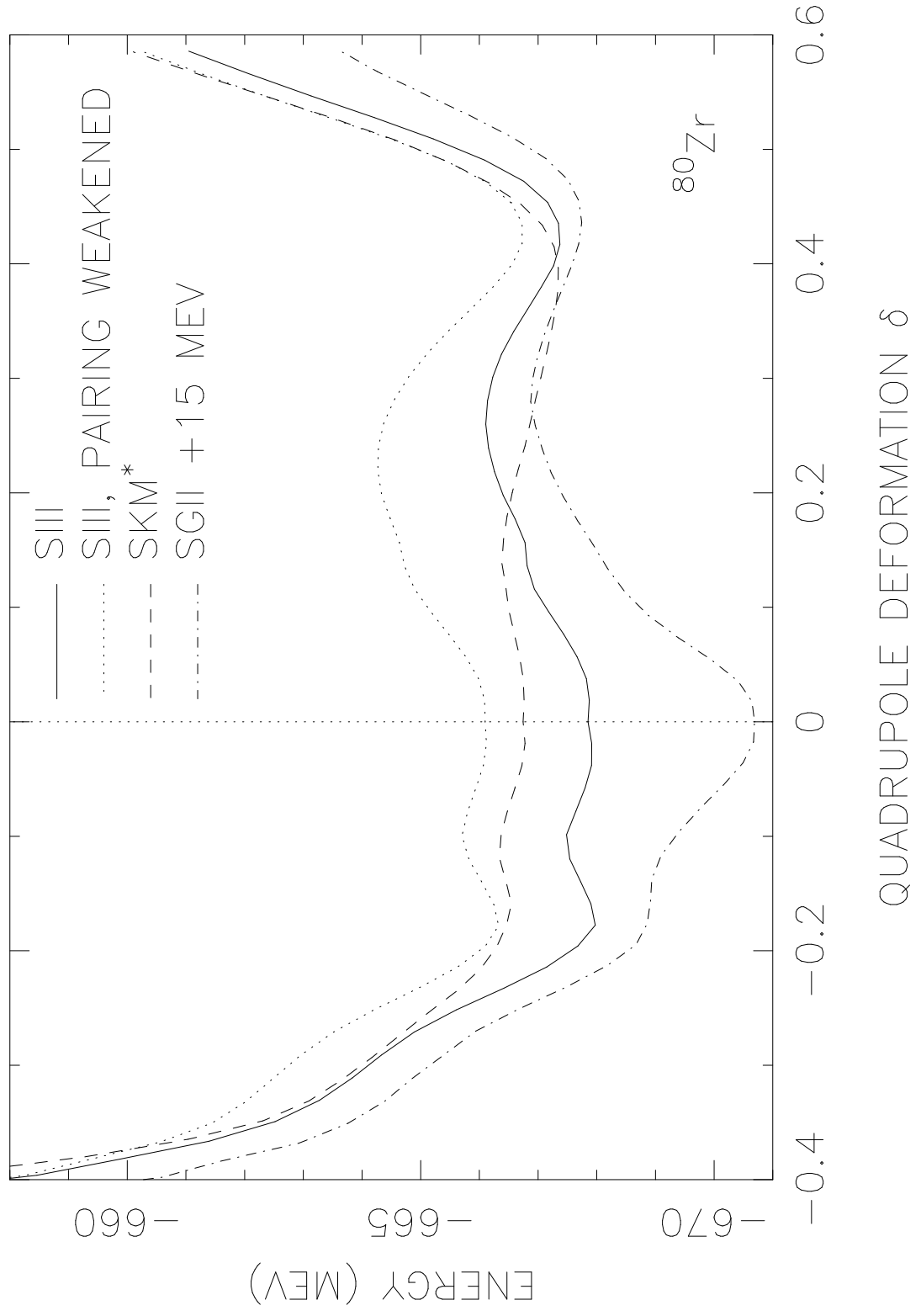


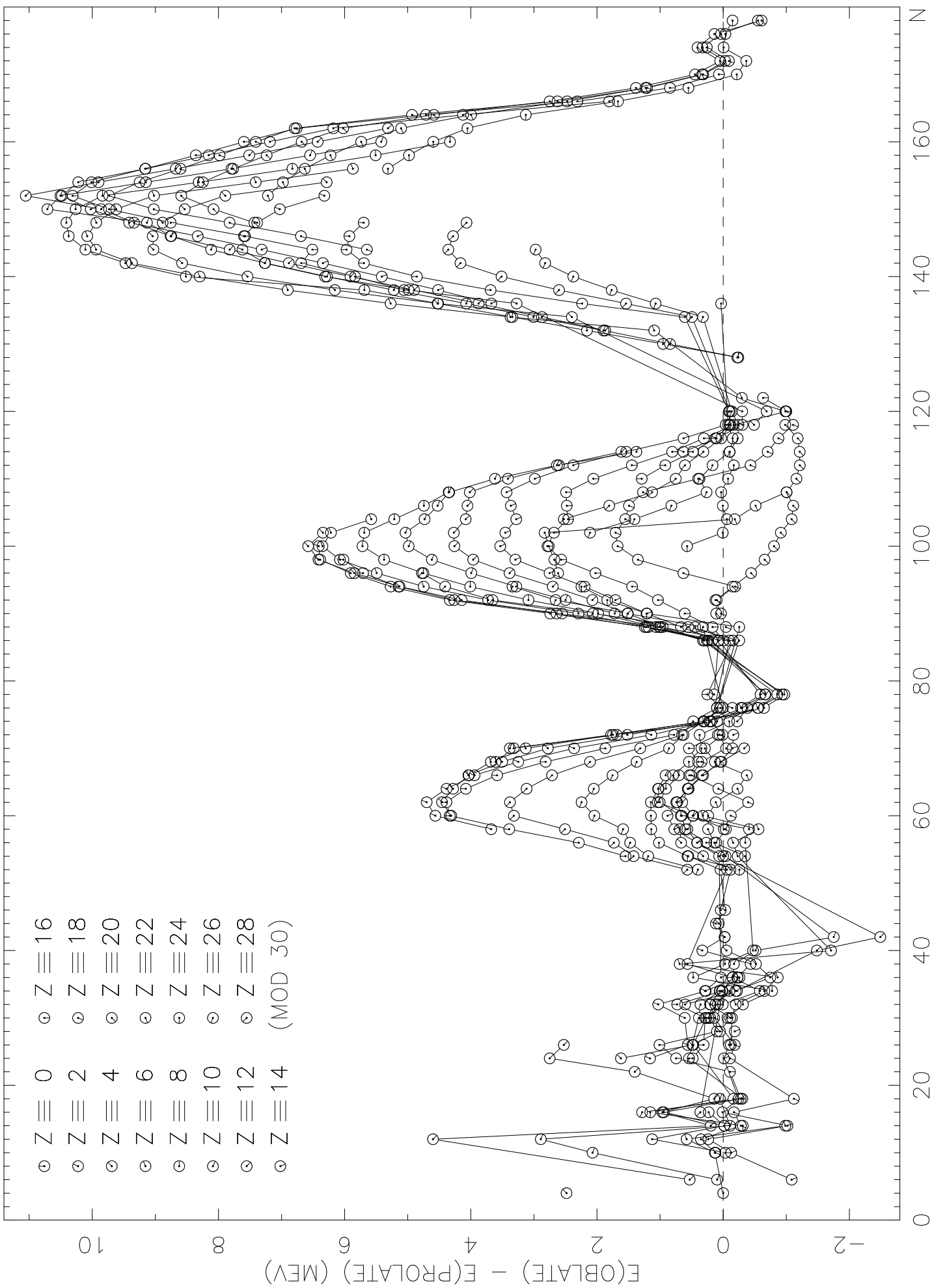


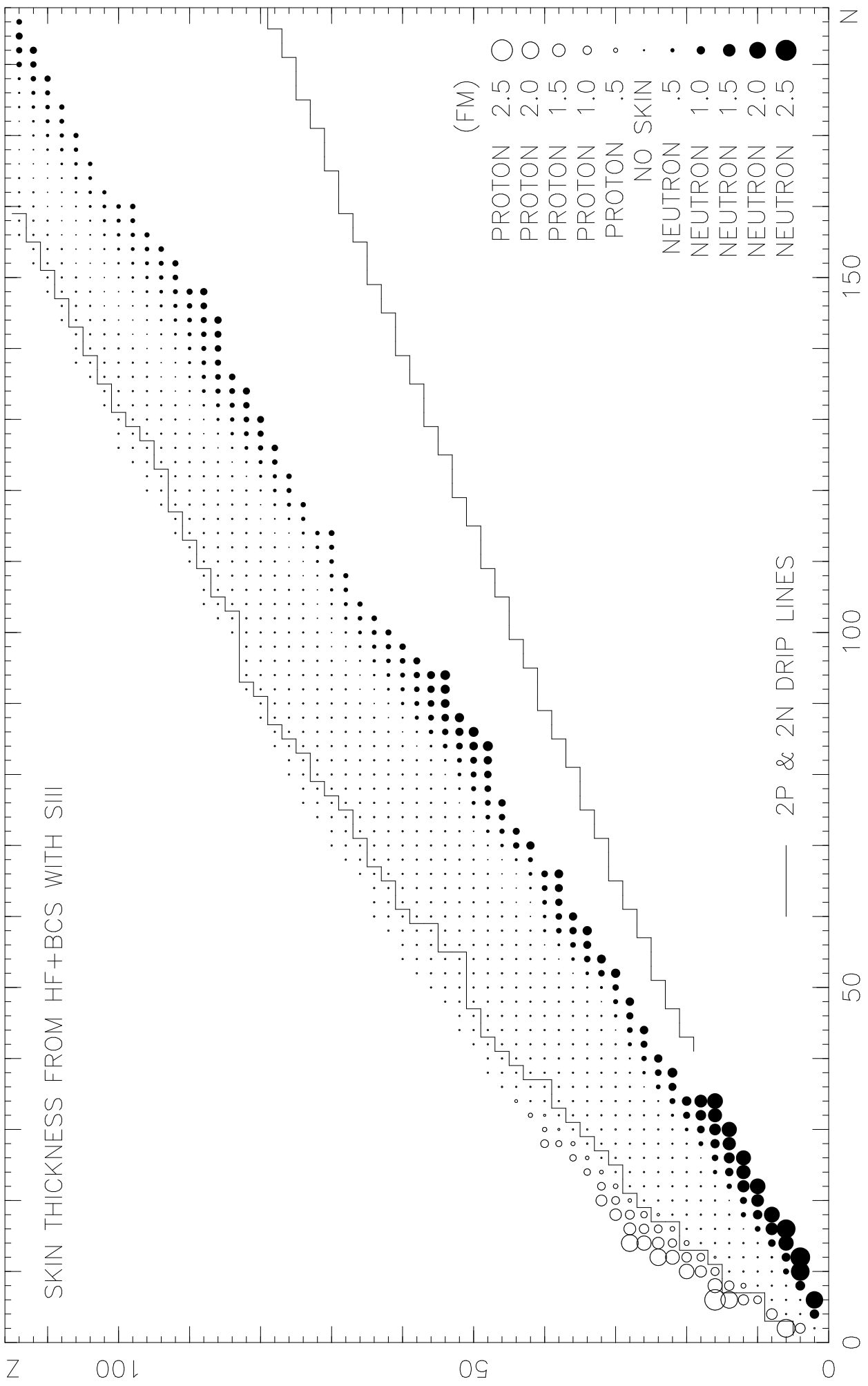


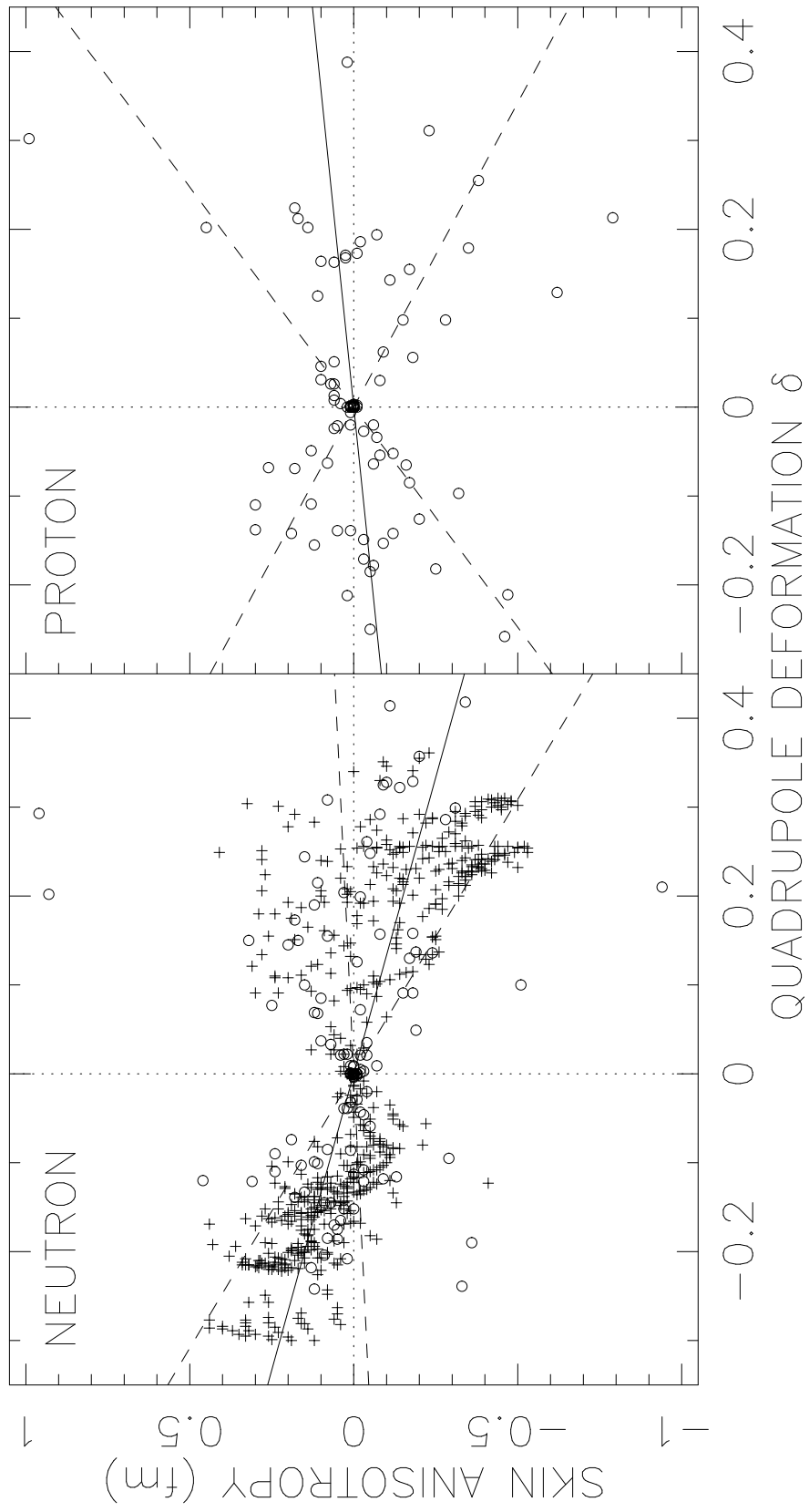


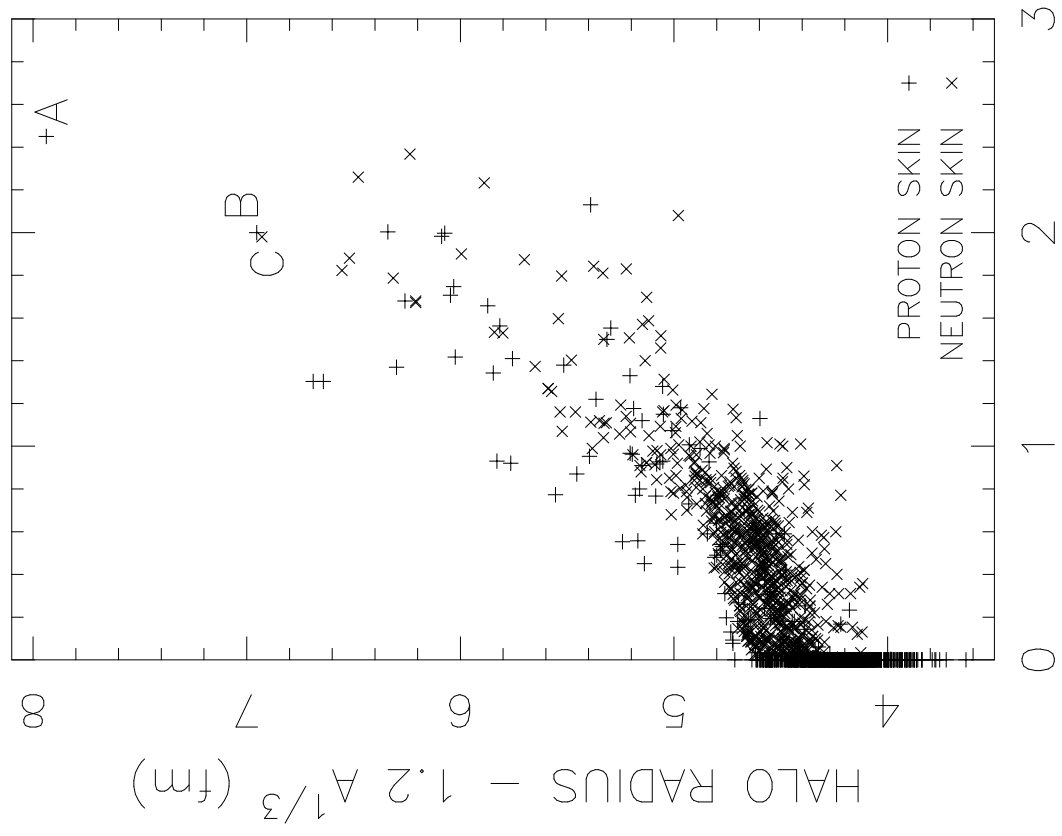












SKIN THICKNESS (fm)